Journal of Energy Chemistry 54 (2021) 528–554

Contents lists available at ScienceDirect

Journal of Energy Chemistry

journal homepage: www.elsevier.com/locate/jechem

http://www.journals.elsevier.com/journal-of-energy-chemistry/

Review

2,5-Furandicarboxylic acid production via catalytic oxidation of 5-hydroxymethylfurfural: Catalysts, processes and reaction mechanism

Chunlin Chen [a,b,c,*], Lingchen Wang [a], Bin Zhu [a,d], Zhenqiang Zhou [a,d], Soliman I. El-Hout [e], Jie Yang [a], Jian Zhang [a,b,c,*]

[a] Ningbo Institute of Materials Technology & Engineering, CAS, 1219 Zhongguan West Road, Ningbo 315201, Zhejiang, China
[b] University of Chinese Academy of Sciences, Beijing 100049, China
[c] Key Laboratory of Bio-based Polymeric Materials Technology and Application of Zhejiang Province, Ningbo 315201, Zhejiang, China
[d] Nano Science and Technology Institute, University of Science and Technology of China, 166 Renai Road, Suzhou 215123, Jiangsu, China
[e] Nanomaterials and Nanotechnology Department, Advanced Materials Division, Central Metallurgical Research and Development Institute CMRDI, Helwan 11421, Egypt

ARTICLE INFO

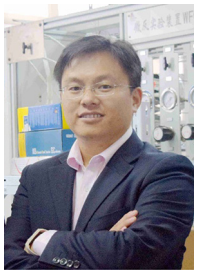
Article history:
Received 31 March 2020
Revised 19 May 2020
Accepted 27 May 2020
Available online 16 June 2020

Keywords:
5-Hydroxymethylfurfural
2,5-Furandicarboxylic acid
Catalytic oxidation
Mechanism

ABSTRACT

Biomass conversion to value-added chemicals has received tremendous attention for solving global warming issues and fossil fuel depletion. 5-Hydroxymethylfurfural (HMF) is a key bio-based platform molecule to produce many useful organic chemicals by oxidation, hydrogenation, polymerization, and ring-opening reactions. Among all derivatives, the oxidation product 2,5-furandicarboxylic acid (FDCA) is a promising alternative to petroleum-based terephthalic acid for the synthesis of biodegradable plastics. This review analytically discusses the recent progress in the thermocatalytic, electrocatalytic, and photocatalytic oxidation of HMF into FDCA, including catalyst screening, synthesis processes, and reaction mechanism. Rapid fundamental advances may be possible in non-precious metal and metal-free catalysts that are highly efficient under the base-free conditions, and external field-assisted processes like electrochemical or photoelectrochemical cells.

© 2020 Science Press and Dalian Institute of Chemical Physics, Chinese Academy of Sciences. Published by ELSEVIER B.V. and Science Press. All rights reserved.



Chunlin Chen received his Ph.D. in Industrial Catalysis in 2013 from the South China University of Technology and the Institute of Metal Research, CAS. Currently, he is an Associate Professor at the Ningbo Institute of Materials Technology & Engineering, CAS. His research focuses on carbon nanomaterials and heterogeneous catalysis.



Lingchen Wang received her M.S. degree in 2018 from the Ningbo Institute of Materials Technology & Engineering, CAS and the Shanghai University. Currently, she is a Process Integration Engineer in the Taiwan Semiconductor Manufacturing Company, Ltd.

* Corresponding authors at: Ningbo Institute of Materials Technology & Engineering, CAS, 1219 Zhongguan West Road, Ningbo 315201, Zhejiang, China.
E-mail addresses: chenchunlin@nimte.ac.cn (C. Chen), jzhang@nimte.ac.cn (J. Zhang).

https://doi.org/10.1016/j.jechem.2020.05.068
2095-4956/© 2020 Science Press and Dalian Institute of Chemical Physics, Chinese Academy of Sciences. Published by ELSEVIER B.V. and Science Press. All rights reserved.



Bin Zhu received his Bachelor degree from the Hefei University of Technology in 2017. He is currently pursuing his Master degree in Chemical Engineering at Ningbo Institute of Materials Technology & Engineering, CAS. His research work focuses on biomass conversion using electrochemical approaches.



Zhenqiang Zhou received his Bachelor degree from the Shandong Agricultural University in 2017. He is currently pursuing his Master degree in Materials Engineering at Ningbo Institute of Materials Technology & Engineering, CAS. His research work focuses on biomass conversion using electrochemical approaches.



Soliman I. El-Hout received his Ph.D. in 2018 in Physical Chemistry through a Joint program from The University of Suez, Egypt and the University of Okayama, Japan. Currently, he is an Assistant Professor at Nanostructured and Nanotechnology Division, Advanced Materials Department, Central Metallurgical R &D Institute, Egypt. His current research interests are in the synthesis of carbon-based nanocomposites for energy storage, water splitting, and heterogeneous catalysis.



Jie Yang received her M.S. degree from China University of Petroleum (Hua Dong) in 2015. She currently works as an engineer at the Ningbo Institute of Materials Technology & Engineering, CAS. Her research work focuses on the aerobic oxidation of 5-hydroxymethylfurfural.



Jian Zhang received his Ph.D. in 2006 from the Dalian Institute of Chemical Physics, CAS, and then moved to the Fritz Haber Institute (FHI) of the Max Planck Society as a postdoctoral fellow and project leader in the Department of Inorganic Chemistry. Currently, He is a Professor at the Ningbo Institute of Materials Technology & Engineering, CAS. His research interests include carbon nanomaterials, metal-free catalysis, and environmental catalysis.

1. Introduction

Both drastic depletion of fossil resources and carbon emission reduction have stimulated considerable efforts to explore new renewable energy. Biomass as a sustainable energy and substance resource is chiefly derived from carbon dioxide fixed by the plant photosynthesis [1–4]. One crucial route of biomass conversion is to transform the plentiful and cheap hexoses (glucose and fructose) into important platform chemicals. 5-hydroxymethylfurfural (HMF), a versatile intermediate dehydrated from abundant C_6 carbohydrates, can be converted to high value-added chemicals (Scheme 1) by oxidation, hydrogenation, polymerization, and ring-opening reactions of its furan ring, aldehyde and alcohol groups [5,6]. For instance, the oxidation products of HMF comprise 2,5-diformylfuran (DFF), 5-hydroxymethyl-2-furan carboxylic acid (HMFCA), 5-formyl-2-furancarboxylic acid (FFCA) and 2,5-furandicarboxylic acid (FDCA), which could be widely used in fine chemicals, pharmacy, chiral catalysis, molecular recognition, and polymers [7–10]. Especially, as one of the top-12 value-added platform chemicals from biomass listed by the U.S. Department of Energy, FDCA is able to make up of the terephthalic acid, a large-scale monomer of the commercial polyethylene terephthalate [4,11–13].

Oxidation of HMF can be carried out by stoichiometric reaction with strong oxidants like potassium permanganate, but this often led to both consumed feedstock and waste residue. The catalytic oxidation route can significantly reduce the reactive energy barrier to allow the reaction going ahead under mild reaction conditions. Meanwhile, the reaction pathway can be modulated by optimizing the catalyst components to reach a high yield of one target product. Extensive efforts have been made to optimize catalyst structure with the gradually becoming clear comprehension of the reaction mechanism, but present catalytic technologies still cannot meet the strict requirements of chemical industries. Regardless, an environmentally friendly route by using water as the solvent and oxygen or air as oxidants is considered as the most attractive choice. This review aims to give a general overview of development and challenges to promote the industrial production of FDCA from HMF oxidation.

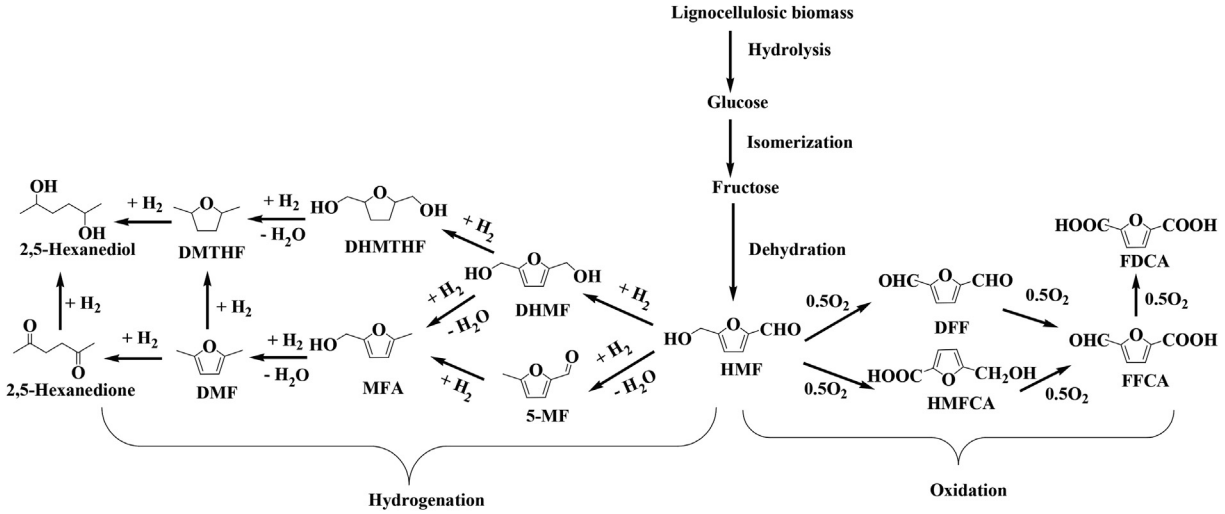
2. Thermocatalytic oxidation of HMF into FDCA

Literature survey shows that the first work about FDCA production was conducted by Fittig and Heinzelmann in 1876 [12,14]. Aqueous HBr was used as both catalyst and solvent to dehydrate mucic acid (Scheme 2a), but this method was restricted by serious corrosion of equipment, poor selectivity, and low FDCA yield. In 1951, Kuhn and co-workers [15] proposed a prospective route to synthesize FDCA in the acidic medium by using an uncommon conjugated hexose derivative as the reactant (Scheme 2b). Recent concerns on environmental protection and the atomic economy motivated a large number of researches on the catalytic oxidation of HMF that is derived from easily available carbohydrates like glucose, fructose, agar or cellulose. Especially, a pilot-plant demonstration with an annual productivity being up to 10,000 tons of HMF was recently completed by Ningbo Institute of Materials Technology and Engineering, Chinese Academy of Sciences in cooperation with Zhejiang Sugar Energy Technology Co., Ltd [16].

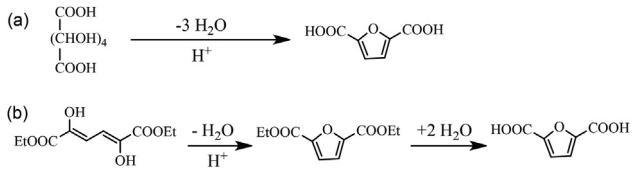
2.1. Liquid alkali system

2.1.1. Single noble metal catalysts

For FDCA production via catalytic oxidation of HMF, the choice of O_2 or air as oxidant show economical and environmental advan-



Scheme 1. The possible pathways of high value-added chemicals from biomass [5,6]. Copyright 2017, The Royal Society of Chemistry. Copyright 2013, Elsevier.



Scheme 2. Synthesis of FDCA from hexose derivates [9,14,15]. (a) Mucic acid route, (b) conjugated hexose route.

tages, which is highly consistent with the direction of sustainable development and the concept of green chemistry. As oxygen is not easily activated, noble metals (Au, Pt, Pd, and Ru) are often selected as heterogeneous catalysts for many oxidation processes including aerobic oxidation of alcohols, aldehydes, cyclohexane, and acrolein, due to their excellent ability to activate molecular oxygen (O_2) [3]. In this section, liquid-phase oxidation systems employed green and clean oxidant together with single noble metal catalysts in nontoxic water are summarized. The critical reaction parameters over each catalyst reported recently are presented in Table 1. Many studies and reviews revealed that Au catalysts are more active for the oxidation of aldehyde groups, whereas Pt and Pd catalysts are more active for the oxidation of alcohol groups [12,17–19]. It is profoundly meaningful to reveal the differences in catalytic activity, giving guidance for the audiences to choose active metal species. Although the reaction rates based on the molar noble metal are precise to describe the specific activity of catalysts, the structural parameters, including particle size, dispersion degree, and exposed facets, have significant influences on catalytic performance. Aim to screen active catalysts for the potential industrial production of FDCA, it is more appropriate to compare specific activity based on the mass of catalysts. Fig. 1 illustrates a comparison of reaction rates for HMF conversion and FDCA generation over all the supported catalysts presented in Table 1. Apparently, Pt catalysts are the most active catalysts, especially in low-temperature condition. Carbon supported Pd catalysts also show remarkable low-temperature activities, while Au catalysts tend to be applied at high temperatures for higher performances. This trend is consistent with the earlier comparative study, which demonstrated that Pt and Pd catalysts were more selective towards FDCA with 79% and 71% selectivity respectively, while Au catalysts required higher O_2 pressures and base concentrations as well as much longer reaction time to reach the similar FDCA selectivity [17]. According to Fig. 1, Ru catalysts show low reaction rates in terms of HMF conversion and FDCA production though they run in higher temperatures, indicating their mass activities need to be improved. Nevertheless, Ru catalysts remain economically attractive because of their low price, usually as low as ~ 4% of that of Au and Pt costs per gram [20]. On the other hand, for a given noble metal, differences in activity arise mainly from the effect of the basic additives and the structural parameters of catalysts, as discussed in detail below.

Efficiently catalytic oxidation of HMF to FDCA usually requires a certain amount of base (e.g. NaOH, $NaHCO_3$, K_2CO_3) whose concentration significantly affects the yield of FDCA. Gorbanev et al. [18] found that the selectivities to both fully oxidized product FDCA and intermediate product HMFCA depended on the amount of added base. The yield of HMFCA was high relative to FDCA at full HMF conversion with low amounts of NaOH, whereas the conversion of HMF was only 13% with 12% HMFCA and 1% FDCA yields in the absence of the base. In the presence of an excess base, a 1 wt % Au/TiO_2 catalyst could oxidize HMF into FDCA with 71% yield at 30 °C and 2 MPa oxygen for 18 h. Casanova and co-workers [21] obtained a nearly 100% yield of FDCA (65–130 °C, 1 MPa air, 8 h) using $Au\text{-}CeO_2$ or $Au\text{-}TiO_2$ catalysts with a molar ratio NaOH/HMF of 4. Besides the single oxide supports, HY zeolite supported Au nanoclusters exhibited a superior performance at a lower oxygen pressure and gave > 99% yield of FDCA under mild conditions (60 °C, 0.3 MPa O_2) [22]. The authors concluded that the HY zeolite supercage restricted the agglomeration of Au nanoclusters and resulted in a modified electronic structure of Au nanoparticles by the interaction with the hydroxyl groups in the supercage. Interestingly, Davis et al. [17] found that, at low pH value, the supported Au catalysts mainly produced HMFCA with a high yield while carbon-supported Pt and Pd catalysts tended to generate FDCA. Increasing the NaOH concentration facilitated the further oxidation of HMFCA into FDCA over Au, which manifested that OH^- could regulate the evolution of HMF as well as the product distribution. Similarly, Strasser and Vuyyuru evaluated the activity of a heterogeneous electrochemical Pt catalyst for HMF oxidation [23], and they observed that the oxidation of the hydroxyl group of HMF was easy at lower pH ($\leq$7) but served as the rate-determining step at higher pH ($\leq$13). Beyond the role in the neutralization of the produced FDCA which otherwise will strongly adsorb on the metallic surface and thus arouse the deactivation, bases facilitate the hydration of –CHO group to form geminal diol intermediate for further oxidative dehydrogenation to the final –COOH. By detailedly analyzed the influence of base in Pt/C medi-

Table 1
Catalytic performance of HMF oxidation into FDCA over single noble metal catalysts.

Catalysts	HMF	T[a]	t[b]	Base (in H_2O)	Oxidant[c]	Conversion[d]	Yield	Reaction rate		Ref.
	(mM)	(°C)	(h)			(%)	(%)	(mmol g_{cat}^{-1} h^{-1})		
								HMF	FDCA	
Au based catalysts										
1 wt% Au/TiO_2	100	30	18	5 equiv. NaOH	2 MPa O_2	100	71	0.282	0.200	[18]
2.6 wt% Au/CeO_2	150	65	8	4 equiv. NaOH	1 MPa air	100	99	2.467	2.442	[21]
Au/HY	543.5	60	6	4 equiv. NaOH	0.3 MPa O_2	99	99	1.375	1.375	[22]
Au-Ce	37.4	95	6	4 equiv. NaOH	1 MPa O_2	100	51.6	1.900	0.981	[46]
2.1 wt% Au/CeO_2	80	140	15	0.2 equiv. Na_2CO_3	0.5 MPa O_2	99.9	91	0.533	0.485	[47]
1.6 wt% Au/ZrO_2_dp	100	125	5	4 equiv. NaOH	0.5 MPa air	100	89	6.061	5.394	[48]
0.57 wt% Au/CeO_2-rod	25	130	2.5	4 equiv. NaOH	0.5 MPa O_2	100	88	4.630	4.074	[49]
2.0 wt% Au/GC	16	110	6	5 equiv. NaOH	0.7 MPa O_2	99.9	97	1.148	1.115	[50]
1.64 wt% Au/Al_2O_3	80	70	4	4 equiv. NaOH	1 MPa O_2	100	99	2.083	2.063	[51]
1.5 wt%Au_3Cu_1/TiO_2	NA[e]	95	4	4 equiv. KOH	1 MPa O_2	100	~98	0.032	0.031	[35]
1.5 wt%Au_3Cu_1/TiO_2	NA[e]	70	4	4 equiv. KOH	1 MPa O_2	100	~42	0.032	0.013	
1.5 wt%Au_1Cu_1/TiO_2	NA[e]	70	4	4 equiv. KOH	1 MPa O_2	100	~27	0.060	0.016	
Pt based catalysts										
3.3 wt% Pt/ZrO_2	100	100	12	2 equiv. $NaHCO_3$	4 MPa air	100	95	1.411	1.340	[37]
Pt-Bi/ZrO_2 (Bi/Pt = 0.25)	100	100	6	2 equiv. Na_2CO_3	4 MPa air	>99	97	2.200	2.156	
Pt-Bi/TiO_2 (Bi/Pt = 0.22)	100	100	4	2 equiv. Na_2CO_3	4 MPa air	>99	99	4.315	4.315	
3.6% Pt_{imp} /C_{L3S}	0.1	100	3	4 equiv. $NaHCO_3$	0.4 MPa air	99	81	6.188	5.063	[24]
5.1% Pt_{imp} 1% Bi/C_{3SW}	100	120	2	2 equiv. Na_2CO_3	4 MPa air	100	>99	13.077	12.946	
3.04 wt% Pt/C	150	22	6	2 equiv. NaOH	0.69 MPa O_2	100	79	3.893	3.076	[17]
Pt/C	158.7	25	2	4 equiv. NaOH	0.1 MPa O_2	100	81	12.819	10.383	[36]
Pt-Pb/C	158.7	25	2	4 equiv. NaOH	0.1 MPa O_2	100	99	12.819	12.691	
1 wt% $Pt/Ce_{0.8}Bi_{0.2}O_{2-\delta}$	150	23	0.5	4 equiv. NaOH	1 MPa O_2	100	98	20.513	20.103	[38]
5 wt% Pt/Fe_3O_4/rGO	25	95	0.5	4 equiv. KOH	0.5 MPa O_2	98.2	38.8	50.359	19.897	[42]
Pd based catalysts										
2.9 wt% Pd/C	150	22	6	2 equiv. NaOH	0.69 MPa O_2	100	71	6.811	4.835	[17]
PVP-Pd NPs	20	90	7	5 equiv. NaOH	0.1 MPa O_2	100	90	32.423	29.181	[25]
$Pd/ZrO_2/La_2O_3$	20	90	8	5 equiv. NaOH	0.1 MPa O_2	99	90	0.454	0.413	[26]
$Pd/KF/Al_2O_3$	20	90	8	5 equiv. NaOH	0.1 MPa O_2	99	91	0.697	0.641	
Pd/Al_2O_3	20	90	8	5 equiv. NaOH	0.1 MPa O_2	99	78	0.521	0.411	
Pd-NOs (6 nm)	20	90	4	4 equiv. $NaHCO_3$	0.1 MPa O_2	100	91.3	9.091	8.300	[27]
Pd-MnO_2	6	100	4	4 equiv. K_2CO_3	0.1 MPa O_2	100	88.1	1.587	1.398	[29]
$Pd/CaMn_2O_4$	40	100	3	2 equiv. Na_2CO_3	0.1 MPa O_2	100	96.8	0.720	0.697	[31]
4.18 wt% Pd/HPGS	200	50	6	1 equiv. NaOH	0.1 MPa O_2	99.96	83.15	3.913	3.255	[30]
20 wt% Pd/CC	158	140	30	3 equiv. K_2CO_3	0.1 MPa O_2	100	85	1.317	1.119	[52]
γ-Fe_2O_3@HAP-Pd (0)	50	100	6	0.5 equiv. K_2CO_3	0.1 MPa O_2	97	92.9	1.617	1.548	[39]
C-Fe_3O_4-Pd	50	80	4	0.5 equiv. K_2CO_3	0.1 MPa O_2	98.2	91.8	1.637	1.530	[40]
Pd/C@Fe_3O_4	50	80	6	2 equiv. K_2CO_3	0.1 MPa O_2	98.4	86.7	1.640	1.445	[41]
Ru based catalysts										
Ru_{imp} /AC	52.9	100	48	4 equiv. $NaHCO_3$	4 MPa air	100	93	0.860	0.800	[34]
Ru/Al_2O_3	100	140	NA[e]	1 equiv. Na_2CO_3	0.3 MPa O_2	99.9	62.9	-	-	[53]
Ru/C	926.7	130	12	2 equiv. $NaHCO_3$	4 MPa O_2	100	93	1.782	1.657	[54]
$ZnFe_{1.65}Ru_{0.35}O_4$	166.7	130	4	1 equiv. K_2CO_3	0.1 MPa O_2	59.3	28.8	0.741	0.360	[43]

[a] reaction temperature
[b] reaction time
[c] reaction oxidant and pressure
[d] conversion of HMF
[e] not available

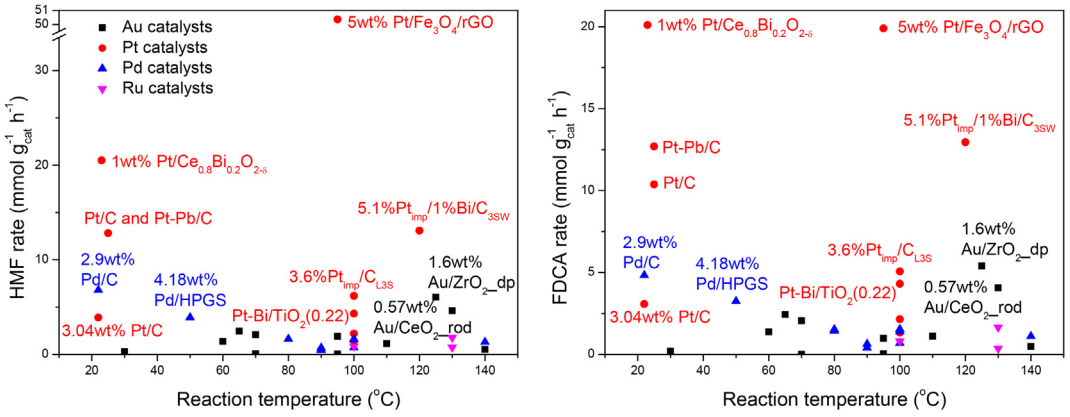


Fig. 1. Reaction rates for HMF conversion and FDCA formation over the supported Au, Pt, Pd, and Ru catalysts.

ated HMF oxidation, Rass et al. [24] pointed out that the higher strength of bases led to a higher catalytic performance in moderately basic aqueous solutions. When choosing NaOH as a base with high concentration, the reaction solution became heavily colored from the beginning, suggesting that HMF suffered from severe degradation. The blank experiments indicated that the degradation of HMF in basic solution was almost inevitable even using the moderate Na_2CO_3. The degradation and selective oxidation of HMF become competitive and affect the yield of the desired product. Most of the noble metal catalysts can rapidly convert HMF to the oxidized intermediates due to their high activity to surpass the degradation to achieve a high FDCA yield; in addition, the catalytic reaction over noble metal catalysts often operated at a lower temperature and in a shorter time course, further mitigating the adverse effects of HMF degradation. However, for the otherwise catalysts with lower activity, such as cheap metals, carbon-based catalysts, as well as some non-optimized noble metal catalysts, strong alkaline will result in a more serious degradation due to the elevated temperature and extended time. Thus, the relatively weaker bases ($NaHCO_3$, Na_2CO_3) were widely employed in these systems. Fig. 2(a) further demonstrates that the choices preference of soluble bases in the HMF oxidation reactions listed in Tables 1–3 were closely correlated with reaction time and temperature, although determined primarily by the activity of catalysts.

The structural parameters of catalysts like particle size, exposed crystal planes, and metal-support interaction have obvious effects

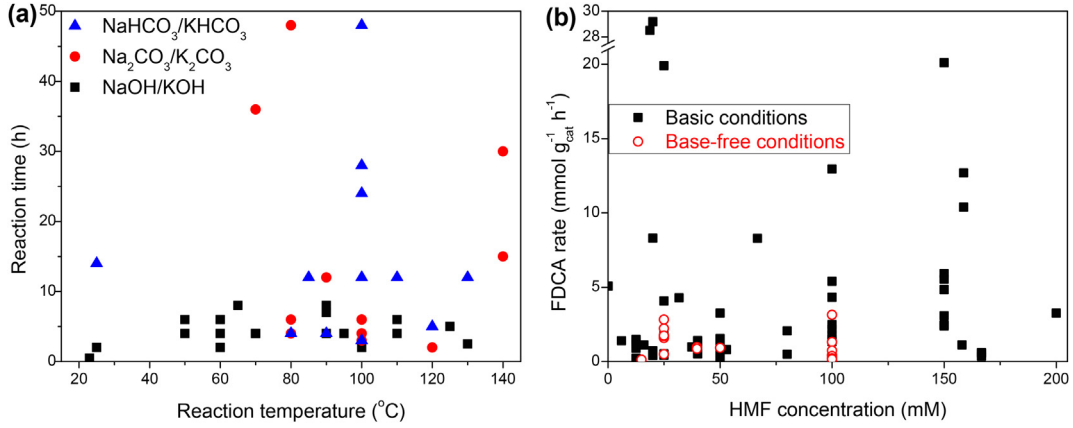


Fig. 2. The influence of alkali. (a) The choices preference of bases for the system with FDCA yield of > 80% under different reaction times and temperatures. (b) FDCA productivity as a function of HMF concentration over noble metal catalysts in alkaline (with soluble and solid bases) and base-free conditions.

Table 2
Catalytic performance of HMF oxidation into FDCA over dual noble metal catalysts.

Catalysts	HMF	T[a]	t[b]	Base (in H_2O)	Oxidant[c]	Conversion[d]	Yield	Reaction rate		Ref.
	(mM)	(°C)	(h)			(%)	(%)	(mmol g_{cat}^{-1} h^{-1})		
								HMF	FDCA	
Au_6-Pd_4/AC	150	60	2	2 equiv. NaOH	0.3 MPa O_2	>99	95	6.158	5.909	[56]
Au_8-Pd_2/AC	150	60	2	2 equiv. NaOH	0.3 MPa O_2	>99	99	5.534	5.534	
Au_6-Pt_4/AC	150	60	4	2 equiv. NaOH	0.3 MPa O_2	>99	94	2.523	2.396	
Au_8-Pt_2/AC	150	60	4	2 equiv. NaOH	0.3 MPa O_2	>99	97	2.518	2.467	
$Au_{0.5}Pd@Co_3O_4$[e]	18.75	90	1	NaOH + Na_2CO_3	H_2O_2	100	95	30	28.5	[58]
Au_6Pd_1-TiO_2	NA[f]	70	4	2 equiv. NaOH	1 MPa O_2	100	85	2.037	1.732	[59]
Au_6@Pd_1 NPs	NA[f]	70	4	2 equiv. NaOH	1 MPa O_2	100	~60	135.870	~81.522	
Pd_1@Au_6 NPs	NA[f]	70	4	2 equiv. NaOH	1 MPa O_2	100	~75	209.486	~157.114	
Au_9Pd_1-TiO_2	NA[f]	90	4	2 equiv. NaOH	1 MPa O_2	100	~87	1.996	~1.736	[60]
Au_1Pd_1-TiO_2	NA[f]	90	4	2 equiv. NaOH	1 MPa O_2	100	~23	2.475	~0.569	
Au_1Pd_3-TiO_2	NA[f]	90	4	2 equiv. NaOH	1 MPa O_2	100	~12	2.906	~0.349	
NYL + TiO_2 + AuPd	18	110	4	2 equiv. NaOH	1 MPa O_2	100	67	-	-	[61]
Au_1-Pd_1/ZOC	50	80	4	4 equiv. $NaHCO_3$	0.3 MPa O_2	>99	>99	3.257	3.257	[62]
Au_1-Pd_1@PECN	50	90	12	4 equiv. K_2CO_3	0.1 MPa O_2	99.7	99	0.763	0.757	[64]
Au_1-Pd_1@PDCN	50	90	12	4 equiv. K_2CO_3	0.1 MPa O_2	88.1	20.3	0.645	0.149	
Au_1-Pd_1@PDECN	50	90	12	4 equiv. K_2CO_3	0.1 MPa O_2	98.6	68.7	0.522	0.364	
Au_1-Pd_1@PEGDCN	50	90	12	4 equiv. K_2CO_3	0.1 MPa O_2	89	35.5	0.515	0.205	
Au_1-Pd_1@PECN-S(PVP)	50	90	12	4 equiv. K_2CO_3	0.1 MPa O_2	99.1	95.4	0.795	0.765	
Pd-Au/HT (1:4)	31.7	60	6	2 equiv. NaOH	0.1 MPa O_2	100	81	5.286	4.282	[65]
$Au_{75}Pd_{25}/TiO_2$-B	40	70	4	2 equiv. NaOH	1 MPa O_2	100	90	1.432	1.289	[66]
$Au_{75}Pd_{25}/TiO_2$-C	40	70	4	2 equiv. NaOH	1 MPa O_2	100	94	1.420	1.334	
$Au_{75}Pd_{25}/TiO_2$-C-200	40	70	4	2 equiv. NaOH	1 MPa O_2	100	99	1.420	1.405	

[a] reaction temperature
[b] reaction time
[c] reaction oxidant and pressure
[d] conversion of HMF
[e] reaction condition: 1 equiv. NaOH and 0.5 equiv. Na_2CO_3 as the mixed bases, 1.5 mL of 10% H_2O_2 as the oxidant.
[f] not available

on the reaction turnover frequency [25–32]. Siyo et al. [25] reported that the Pd nanoparticles (NPs) with a mean diameter of 1.8 nm in an alkaline aqueous solution (T = 90 °C, p_{O2} = 0.1 MPa) afforded up to 90% yield of FDCA. The influence of supports on the aerobic oxidation of HMF into FDCA was also studied [26]. Deposited the above 1.8 nm Pd NPs on different metal oxides (TiO_2, γ-Al_2O_3, KF/Al_2O_3, and ZrO_2/La_2O_3), the $Pd/ZrO_2/La_2O_3$ catalyst showed the best catalytic performance (>90% yield of FDCA) and stability with the addition of 2 equivalents(equiv.) of $NaHCO_3$. Liu et al. [27] studied the facet effect of single-crystalline Pd nanocrystals through experimental and theoretical approaches and pointed out that the catalytic performance was notably controlled by the particle size and exposed facet of Pd nanocrystals. The (111)-faceted Pd nanooctahedrons (Pd-NOs) were more active than (100)-faceted nanocubes (Pd-NCs) especially in the conversion of HMF to HMFCA and FFCA. However, the situation is different for the single-crystalline Pt nanocrystals with particle size of sub-10 nm. Yu et al. [28] found that Pt-NCs enclosed by the (100) facets exhibited higher catalytic activity compared with Pt-NOs enclosed by the (111) facets and Pt nanospheres (Pt-NSs), mainly due to the fact that •OH created on Pt(100) facet is more active for the dehydrogenation of HMFCA to form FFCA compared with the $^{\bullet}O_2$ generated on Pt (111) facet. Recently, Jiang et al. [29] found that the activity in the productivity of FDCA by the atomic Pd catalyst supported on MnO_2 was over twice that of its Pd nanoparticle counterpart. The experimental and theoretical results revealed that the high dispersion of atomic Pd maximized the metal-support interactions and tuned the electronic properties of active sites, thus enhancing their binding affinity to the HMF molecules. Our group also successfully developed highly porous

Table 3
Catalytic performance of HMF oxidation into FDCA over cheap metal and carbon-based catalysts.

Catalysts	HMF	T[a]	t[b]	Base (in H_2O)	Oxidant[c]	Conversion[d]	Yield	Reaction rate		Ref.
	(mM)	(°C)	(h)			(%)	(%)	(mmol g_{cat}^{-1} h^{-1})		
								HMF	FDCA	
$SrMnO_3$	40	100	24	3 equiv. $NaHCO_3$	1 MPa O_2	99	58	0.083	0.048	[70]
MnO_2	40	100	24	3 equiv. $NaHCO_3$	1 MPa O_2	99	91	0.083	0.076	
activated MnO_2	40	100	24	3 equiv. $NaHCO_3$	1 MPa O_2	99	74	0.165	0.123	[71]
β-MnO_2-HS	40	100	24	2 equiv. $NaHCO_3$	1 MPa O_2	99	86	0.165	0.143	
holey 2D Mn_2O_3	50	100	24	3 equiv. $NaHCO_3$	1.4 MPa O_2	100	99.5	0.278	0.276	[72]
MnO_x-CeO_2	50	110	12	2 equiv. $KHCO_3$	2 MPa O_2	98.5	88.7	0.410	0.370	[73]
Co-Mn-0.25	50	120	5	2 equiv. $NaHCO_3$	1 MPa O_2	99	95	0.990	0.950	[74]
$MnCo_2O_4$	40	100	24	3 equiv. $KHCO_3$	1 MPa O_2	99.5	70.9	0.083	0.059	[75]
$Mn_{0.75}/Fe_{0.25}$	100	90	24	4 equiv. NaOH	0.8 MPa O_2	90	32	0.775	0.267	[76]
Ni-MnO_x	100	100	28	4 equiv. $NaHCO_3$	0.8 MPa O_2	100	93.8	0.357	0.335	[77]
Co-MnO_x	100	100	28	4 equiv. $NaHCO_3$	0.8 MPa O_2	100	84.5	0.357	0.302	
Fe-MnO_x	100	100	28	4 equiv. $NaHCO_3$	0.8 MPa O_2	100	78.6	0.357	0.281	
MnO_x	100	100	28	4 equiv. $NaHCO_3$	0.8 MPa O_2	100	72.8	0.357	0.260	
commercial MnO_2	100	100	28	4 equiv. $NaHCO_3$	0.8 MPa O_2	100	56.7	0.357	0.203	
Co-Mn/N@C	50	85	12	1 equiv. Na_2CO_3	0.1 MPa O_2	99.7	96.1	0.831	0.801	[78]
$Ce_{0.5}Bi_{0.5}O_{2-\delta}$	150	65	1	4 equiv. NaOH	1 MPa O_2	100	8	9.000	0.720	[55]
(N)-CuO/Al_2O_3 fibers	20.8	50	4	4 equiv. NaOH	0.1 MPa air	100	98.6	1.984	1.956	[80]
CoPz/g-C_3N_4[e]	20	RT[f]	14	$Na_2B_4O_7$ buffer solution	0.1 MPa air	99.1	96.1	11.326	10.983	[81]
CoPz/g-C_3N_4	20	RT[f]	14	$Na_2B_4O_7$ buffer solution	0.1 MPa air	17.5	15.8	2.000	1.806	
CoPz/g-C_3N_4	20	RT[f]	14	$Na_2B_4O_7$ buffer solution	0.1 MPa air	11.5	10.3	1.314	1.177	
$[EMIM]_4Mo_8O_{26}$	200	100	2	2 equiv. NaOH	98.6 mM H_2O_2	99.5	99.5	39.484	39.484	[82]
NNC-900	63	80	48	3 equiv. K_2CO_3	0.1 MPa O_2	100	80	0.066	0.053	[83]
PCN_x	100	70	36	1 equiv. K_2CO_3	0.1 MPa air	100	83	1.389	1.153	[85]

[a] reaction temperature
[b] reaction time
[c] reaction oxidant and pressure
[d] conversion of HMF
[e] under UV–visible light
[f] room temperature

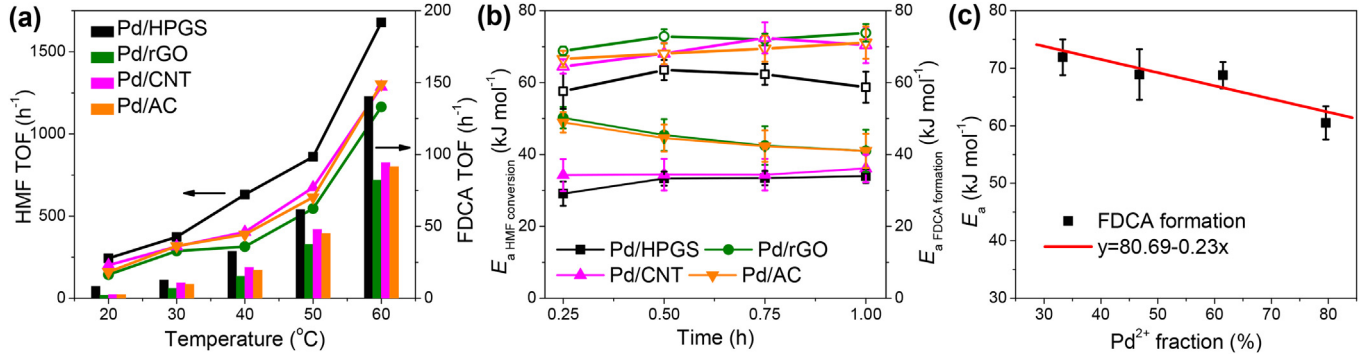


Fig. 3. Kinetic measurements and analysis [30]. (a) TOF (h^{-1}) and (b) E_a (kJ mol^{-1}) obtained within 1 h reaction time. (c) Correlation between activation energies and surface Pd^{2+} fractions over the four catalysts. Copyright 2017, The Royal Society of Chemistry. Copyright 2013, Elsevier.

nitrogen- and phosphorus-codoped graphene sheets (HPGS) supported Pd catalysts under mild conditions. The structure–activity correlation demonstrated that the heteroatoms doped support will enhance the fraction of surface Pd^{2+} species, which plays a crucial role in reducing of the activation energies of both HMF conversion and FDCA formation [30]. Especially, the apparent activation energy (E_a) of FDCA formation exhibited a linear dependency on the fraction of surface Pd^{2+} (Pd^{II}, %), which can be quantitatively described by the equation $E_{a,FDCA}$ = 80.69–0.23 × Pd^{II}. This finding provided a new strategy to develop a highly active catalyst by regulating the interaction between the active component and support toward the energy-saving production of FDCA (Fig. 3).

In view of the high cost of Au, Pd and Pt, researchers began to employ the less expensive Ru as the active phase for HMF oxidation. Liu et al. [33] compared the performances of activated carbon-supported Ru (Ru/C), Pt (Pt/C), Pd (Pd/C) catalysts and metal oxides-supported Ru catalysts (Ru/ZrO_2, Ru/TiO_2, Ru/Al_2O_3), revealing that Ru/C was far superior to the others with much higher FDCA selectivity and carbon balance. The authors also found that the strong basicity of NaOH and Na_2CO_3 facilities the formation of humins via HMF ring-opening and polymerization reactions. Although $Mg(OH)_2$ has low solubility in water (K_{sp} = 1.5 × 10^{11}) to form a suspension, the dissociation of the small amount of its dissolved part is sufficient to act an outstanding basic additive to provide the best performance. Kerdi et al. [34] claimed that Ru nanoparticles supported on nitrogen-containing carbons could catalyze HMF oxidation with a complete conversion and a 93% yield of FDCA in the aqueous $NaHCO_3$. The results highlighted that oxygen-functionalized and amine-functionalized catalyst surface exhibited a detrimental impact on the reaction rate.

To reduce the catalyst costs, cheap metals were often chosen to lower the proportion of noble metal in alloys or serve as cocatalysts or promoters [35]. In 1993, Verdeguer et al. [36] reported that FDCA yield increased from 81% to 99% after merging Pb into Pt/C catalyst. Albonetti et al. demonstrated that the catalytic performance of TiO_2 supported Au catalyst was remarkably increased at the presence of Cu, which by itself was not active in the HMF oxidation. The strong effect of Au/Cu atomic ratio in the alloyed bimetallic nanoparticles was observed on catalytic activity and reusability. With the optimum 1.5 wt% total metal loading, the catalyst with Au/Cu ratio of 3 presented the best catalytic activity, while the bimetallic system with Au/Cu ratio of 1 showing the highest level of reusability [35]. Rass et al. exploited non-noble metal Bi as a promoter to prepare Pt-Bi/TiO_2 and Pt-Bi/C catalysts for deep oxidation of HMF to FDCA with > 99% yield using $NaHCO_3$ and $NaCO_3$ at elevated temperatures [24,37]. A Bi/Pt molar ratio of ca. 0.2 accelerated the reaction and partially prevented the catalyst deactivation upon recycling operations. Yang et al. [38] also found that the Bi doping could thoroughly change the catalytic behavior of Pt/CeO_2 in HMF oxidation. The Bi-doped CeO_2 accelerated the oxygen reduction process due to the presence of abundant oxygen vacancies and the cleavage of the peroxide intermediate promoted by bismuth. The unique function was well incorporated with the activity of Pt during the catalytic oxidation cycle, endowing the $Pt/Ce_{0.8}Bi_{0.2}O_{2-\delta}$ catalyst with the best performance yielding 98% of FDCA within 30 min at room temperature.

Heterogeneous catalysis seems to be more favorable than homogenous catalysis due to the easy separation of the catalyst from the reaction suspension system and hence good recyclability of the catalyst. The product solution is filtered or centrifuged for

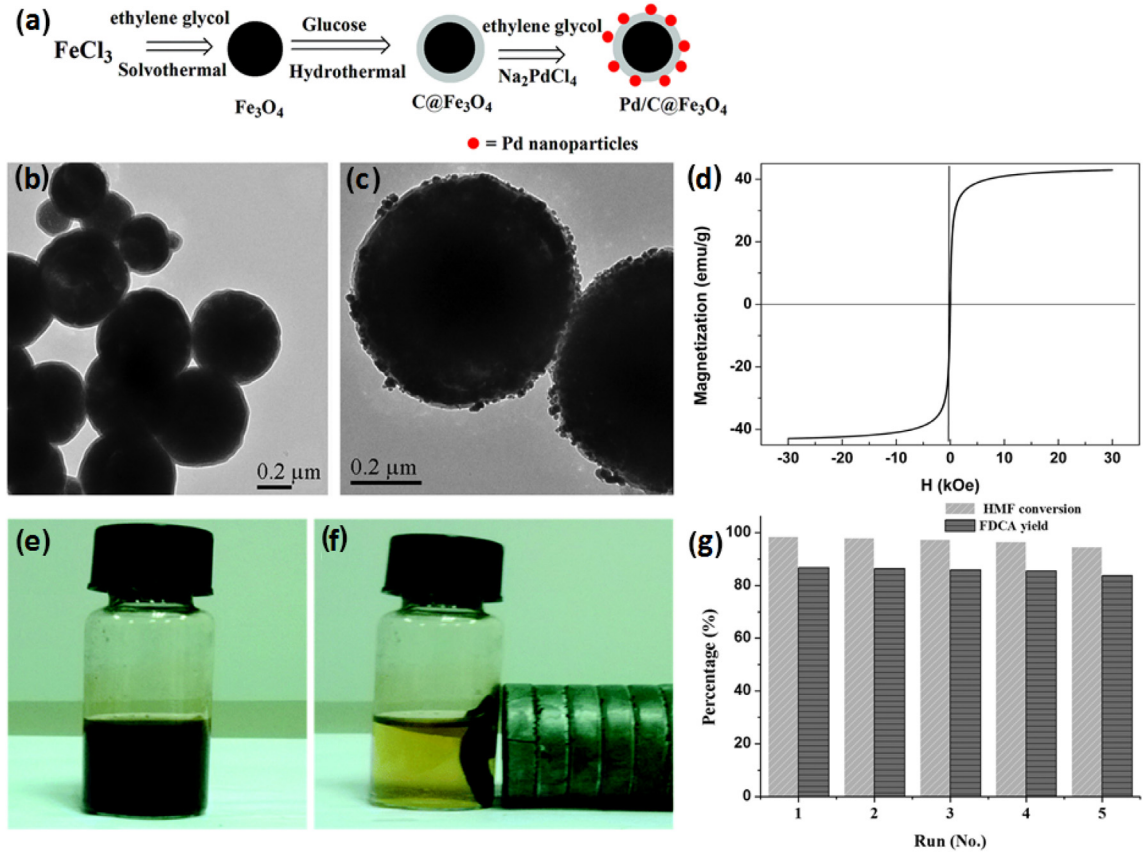


Fig. 4. Magnetic catalysts [40,41]. (a) Schematic diagram of the synthesis of the Pd/C@Fe_3O_4 catalyst. TEM images of the (b) C@Fe_3O_4 microspheres and (c) Pd/C@Fe_3O_4 catalyst. (d) Magnetism of Pd/C@Fe_3O_4 catalyst. Magnetic separation of the C-Fe_3O_4-Pd catalyst: (e) after reaction, (f) after separation by an external magnet. (g) Durability of the Fe_3O_4@C-Pd catalyst. Copyright 2015, The Royal Society of Chemistry.

catalyst separation, and the isolated catalyst is washed with dilute alkali solution and water in sequence and reused for the following run. However, the filtration and centrifugation operations still cause inevitable loss and the waste of rare metal resources as well as more consumption of energy, while the combination with magnetic nanostructures greatly improves the recovering efficiency. Zhang and co-workers [39–41] prepared a series of novel magnetic catalysts using Pd and Fe (γ-Fe_2O_3@HAP-Pd, C-Fe_3O_4-Pd, and Pd/C@Fe_3O_4) for the aerobic oxidation of HMF in water with 0.5 equivalent of a weak base under mild reaction conditions. The highest yield of FDCA reached 93% and the external magnet facilitated the separating of catalyst particles to keep the activity after the fifth run. The purpose of the combination of magnetic Fe_3O_4 and hydrophilia carbon surface is to improve the separation and recovery of the catalyst (Fig. 4). Zhou et al. [42] adopted the analogous strategy to develop a novel Pt nanocatalyst supported on Fe_3O_4 decorated with reduced graphene oxide (Pt/Fe_3O_4/rGO). The results highlighted that the introduction of Fe_3O_4 could increase the dispersion, thus promote the utilization and the catalytic activity of Pt. The activation of –OH and –CHO groups was enhanced at the Pt/Fe_3O_4 interface, providing a twice higher reaction rate as that of Fe_3O_4-free catalyst. After five times of magnetic recycle, Pt/Fe_3O_4/rGO remained relatively stable with Pt loading decreasing from 5.0 wt% to 4.9 wt% and Fe content decreasing from 22.1 wt % to 20.6 wt% as well as a slight deterioration in catalytic performance (7% HMF conversion and 19% FDCA selectivity). Beyond magnetic Fe_3O_4, by partially replacing Fe(III) in spinel-phase $ZnFe_2O_4$ by Ru(III), Qi et al. [43] synthesized a series of trimetallic catalysts with soft magnetic characteristics via a simple alkali-coprecipitation method, albeit the catalytic performance in aqueous phase needed to be improved. Apart from precious metal catalysts, the concept of magnetic separation was expanded to transition metal oxide and immobilized enzyme for the oxidation of HMF, such as magnetic $MnFe_2O_4$ catalyst [44] and laccase catalyst [45], respectively. Table 1 summarizes the catalytic performance of HMF oxidation over single noble metal catalysts.

2.1.2. Dual noble metal catalysts

Owing to the instability of single noble metal catalysts, the active metal atoms are easy to leach out to the reaction mixture and thus the deactivation of the catalyst is usually unavoided, especially with the presence of strong acid or base. In order to enhance the recyclable stability and activity of the single noble metal catalyst in the HMF oxidation reaction to produce FDCA, some researchers have introduced secondary metal as an additive to adjust the electronic properties of the active centers and to form a smaller particle size of the catalyst. Compared to monometallic catalysts, the physical and chemical properties of bi- and multimetallic catalysts may be tuned efficiently by varying the composition, crystalline state, alloying degree, and grain boundary. Numerous bimetallic catalysts based on mixing or alloying Au or Pt with a second non-noble metal were reported with improved catalytic efficiency and stability [24,35,37,38,55]. However, the active sites of these catalysts are relatively too single to meet higher requirements, and it is possible to further improve the catalytic performance by incorporating another active noble metal to strengthen the synergistic effect or accelerate the different fundamental steps. The rational design of multi-component noble metals can indeed combine the advantages of different components and thus harvest much higher efficiency than that obtained by simply mixing the two single noble metal catalysts. As examples of Pt-M [56] and Ru-M (M = noble metal) catalysts are rarely reported in FDCA production, this section focuses on the discussion of Au-Pd catalyst systems.

In 2013, Villa et al. [56] showed that the modification of Au/C catalyst with Pd or Pt generated excellent catalytic efficiency and stability under realistic reaction conditions. AuPd catalysts performed more active than AuPt ones, achieving almost full conversion to FDCA within 2 h and 4 h, respectively, whereas Au catalyst needed 6 h to reach just 80% selectivity. Due to irreversible adsorption of intermediates or Au particle agglomeration rather than Au leaching, Au/C catalyst underwent apparent deactivation, losing 20% of activity after the fifth run. Alloying Au with Pd in an optimal 8:2 atomic ratio endowed the bimetallic catalyst with a more active and stable performance to completely convert HMF with 99% selectivity to FDCA over all five runs. In addition, the conjunction of a second metal to Au-based catalyst can affect the oxidation reaction pathways of HMF. For example, the oxidation pathway of HMF has been changed from HMFCA to DFF by the introduction of Pd to Au/CNT catalyst where Pd active sites support the oxidation of the –OH groups of HMF, and promote the further oxidation of FFCA to FDCA, which is a difficult step for Au catalysts [57]. Very recently, Liao et al. [58] engineered a Co_3O_4 supported catalyst with an active interface between Au-Pd alloy NPs by calcining alloy embedded ZIF-67 metal–organic frameworks for highly efficient conversion HMF to yield 95% of FDCA within 1 h. The time-course composition of reaction systems revealed that the conversions of HMF achieved equally 100% in 10 min, while the yields to HMFCA were 80% and 20% for Au@Co_3O_4 and $Au_{0.5}$-Pd@Co_3O_4, respectively. After 1 h reaction, 50% of HMFCA remained as the main product over Au@Co_3O_4 compared to the almost complete conversion of HMFCA over the Pd modified catalyst within 40 min. On the other hand, Pd@Co_3O_4 and Pd/C were unable to oxidize HMFCA as a reactant. The results suggested that the oxidation of HMFCA was mostly contributed to the Au species and can be promoted by adding Pd into Au NPs to reduce the activation barrier. As a structure–activity relationship, one of the key factors affecting the catalytic performance of HMF-to-FDCA was the increase in the percentage of active Au^+ owing to the size effect. Detailed characterization indicated that the reduced particle size of metal NPs could be attributed to alloying Au with Pd. Albonetti et al. [59–61] synthesized bimetallic Pd-Au nanoparticles with alloy and core–shell structures and found that catalytic reactivities and reaction paths depended on preferentially exposed active phase composition (either Au or Pd atoms). Both monometallic Au and Pd NPs transformed HMF to HMFCA, while the subsequent oxidation of HMFCA to FDCA preferentially occurred on monometallic Au (12%–19% of selectivity to FDCA) or bimetallic Pd-Au catalysts (up to 85% of FDCA selectivity) rather than monometallic Pd NPs (0%–9% of selectivity to FDCA). However, catalysis on the Pd-Au catalyst calcined at 300 °C revealed a decreased selectivity to FDCA to be only 50% after the same 4 h reaction time, whereas the selectivity to HMFCA was constant to about 50% during the whole time. The author ascribed the results to the Pd migration towards the surface to form Pd layer or Pd-rich shell by de-alloying of Au and Pd upon calcination. The highly consistent behavior over bimetallic Au@Pd and Pd@Au catalysts confirmed the speculation again [59]. In particular, for the TiO_2 supported catalysts, as Au content in alloys increasing, the selectivity to FDCA increased in the order of Au_1Pd_3 < Au_1Pd_1 ≪ Au_3Pd_1 < Au_9Pd_1 < Au_6Pd_1 [60], suggesting a synergic effect existed in the bimetallic catalysts. The distribution of reaction products was strongly affected by the Pd:Au atomic ratio due to the fact that a small quantity of Pd was adequate to significantly change the electronic properties of Au and enhance its catalytic activity. The similar synergistic effect between Pd and Au on enhancing the HMF conversion and FDCA selectivity was also validated by Qi et al., where the yield of FDCA increased to > 99% when the Pd:Au molar ratio reached 1:1 [62]. The potential-dependent electrocatalytic oxidation of HMF on supported bimetallic Au-Pd nanoparticles in alkaline media was also explored to reveal a synergistic effect of Au-Pd alloy on the highly selective formation of FDCA [63]. Deeply

oxidized products (FFCA and FDCA) could be produced over bimetallic catalysts at lower potentials with respect to monometallic catalysts. Although the Au-Pd bimetallic catalysts were often reported to be highly active in oxidation of HMF into FDCA [64–66], the synergistic strategy by alloying two or more precious metals will complicate the procedure and push the cost of catalyst even higher. The catalytic performance of HMF oxidation over dual noble metal catalysts are listed in Table 2.

2.1.3. Cheap metal and carbon-based catalysts

The efficient recycling of precious metals is able to suppress the capital cost of the catalytic oxidation process, but developing inexpensive transition metal and metal-free catalysts is always the ultimate goal of the biorefinery industry. The $Co(OAc)_2/Mn(OAc)_2/HBr$ catalyst was firstly introduced into HMF oxidation for industrial production of terephthalic acid by Partenheimer [67,68], but the separation of catalyst and the final product is always one of the challenges in the homogeneous catalytic system. This study inspires extensive research on heterogeneous catalysis based on transition metals. During the investigation on manganese-based heterogeneous oxidation catalysis with O_2 as the sole oxidant [69], Hara's group found that the activated MnO_2 catalyzes the oxidation of HMF to FDCA more efficiently than $SrMnO_3$ in the presence of $NaHCO_3$ as an additive [70]. Interestingly, the comparative experiment under Ar atmosphere revealed that HMF was converted into oxygenated products with almost the same reaction rate as that under O_2 atmosphere. In addition, the reaction rates over MnO_2 were slightly dependent on the pressure of O_2, and doubled when the pressure raised from 0.1 to 1.0 MPa. The authors interpreted such phenomena to the substrate oxidation by oxygen supplied from the catalyst itself (Mars-van Krevelen mechanism). During this process, the formation of partially reduced $MnO_{2-\delta}$ or irreversible MnOOH will affect the stability of MnO_2. Thus, the crystallization is helpful to improve the structural stability of MnO_2. It is well known that MnO_2 has various crystal structures, which was demonstrated to be very crucial to catalytic HMF oxidation to FDCA through combined computational and experimental studies recently by the above research group [71]. Density functional theory (DFT) simulations revealed that the vacancy formation energies at the bent oxygen sites in β- and λ-MnO_2 are lower than those at the planar oxygen sites in α- and γ-MnO_2, suggesting the first two types are likely to be good candidates for the target reaction. Experimental studies, including the kinetic, mechanistic, and spectroscopic investigations, further demonstrated that the reaction rates of the rate-determining step (FFCA → FDCA) decrease in the order of β-MnO_2 > λ-MnO_2 > γ-MnO_2 ≈ α-MnO_2 > δ-MnO_2 > ε-MnO_2. So, Hara's group confirmed that the combined theoretical and experimental approachescan provide a rational strategy to design highly effective MnO_2 catalysts. In addition, the catalytic performance of the β-MnO_2 can be further improved significantly by increasing its surface area [71].

Beyond crystal structure, the diverse oxidation states to form redox pairs of Mn^{2+}/Mn^{3+} or Mn^{3+}/Mn^{4+} also endow manganese oxides with outstanding catalytic properties. Hu et al. [72] combined the redox cycle of the Mn cations with abundant surface pores to develop a holey 2D Mn_2O_3 nanoflakes by the controlled heat-treatment of a Mn-based metal–organic framework (Mn-MOF). The obtained nanoflakes (M400) exhibited outstanding catalytic activity for the aerobic oxidation of HMF to FDCA, significantly outperforming commercial Mn_2O_3 and activated MnO_2 as well as the above Mn-based catalysts in the aspect of reaction rates. In addition, according to the Mars-Van-Krevelen mechanism, oxidation reactions over manganese oxides rely closely upon the oxygen mobility from the external O_2 to the oxide's lattice oxygen to complete the catalytic cycle and regenerate the surface of catalyst (Fig. 5a). Due to its high oxygen storage capacity, CeO_2 was employed by Wang et al. to promote the lattice oxygen transfer from Ce oxide to Mn oxide to enhance the catalytic activity and selectivity [73]. H_2 temperature programmed reduction (H_2-TPR) experiments revealed that the reduction temperature decreased gradually with the increase of Ce proportion, verifying that the oxygen mobility was significantly improved due to the addition of Ce oxides. This study also pointed out the high concentrations of Mn^{4+} and Ce^{3+} on the MnO_x-CeO_2 surface play a key role as active sites for the HMF oxidation. Superior oxygen mobility and various oxidation states are widely accepted to elucidate the remarkable performance of multitudinous Mn-based composites, such as Co-Mn-0.25 [74], $MnCo_2O_4$ [75], and Mn-Fe mixed oxide [76]. Yu et al. [77] further proposed that active $M^{3+}O(\text{-}Mn^{4+})_2$ clusters in (Fe, Co, Ni)-doped MnO_x catalysts were the principal active sites for the aerobic oxidation of HMF (Fig. 5b). This work also provided a universal mechanism based on electron transfer inside the catalytically active sites for binary [78] and ternary metal oxides [79].

Mn-free catalysts were also explored in the past few years. Yang et al. [55] reported 97% of HMF conversion was reached in 20 min at 65 °C and 1 MPa O_2 over $Ce_{1-x}Bi_xO_{2-\delta}$ ($0.08 \le x \le 0.5$), which was attributed to the enhanced O_2 activation by Bi doping. However, only a small amount of FDCA formed with an 8% yield after reaction for 1 h, in spite of the reaction rate for FDCA superior to most of Mn-based catalysts. Li et al. [80] fabricated three CuO/Al_2O_3 catalysts with smooth, porous and needle-like fiber morphologies for

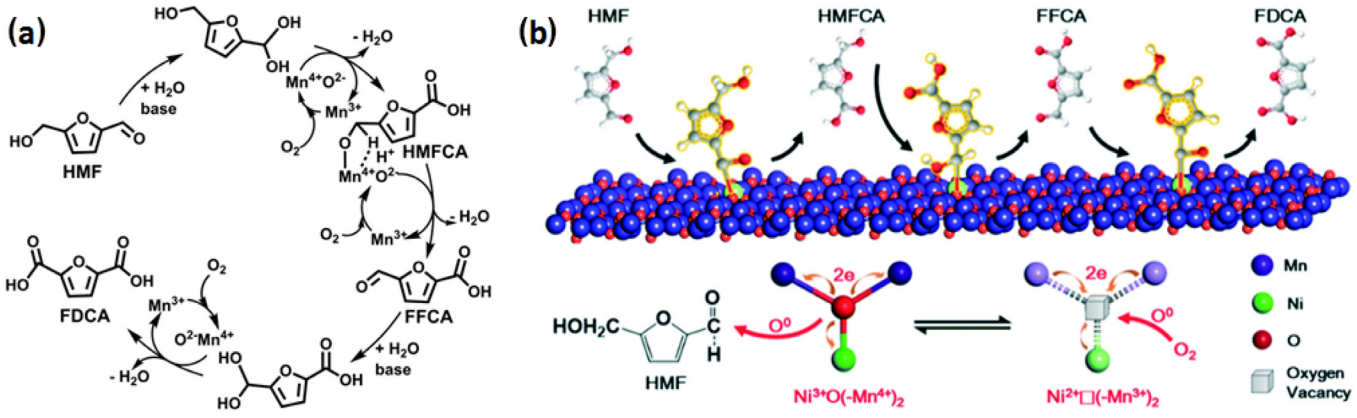


Fig. 5. HMF oxidation into FDCA over (a) unary Mn_2O_3 [72] (Copyright 2019, Wiley-VCH Verlag GmbH & Co. KGaA, Weinheim) and (b) binary Mn-based catalysts [77] (Copyright 2019, Wiley-VCH Verlag GmbH & Co. KGaA, Weinheim).

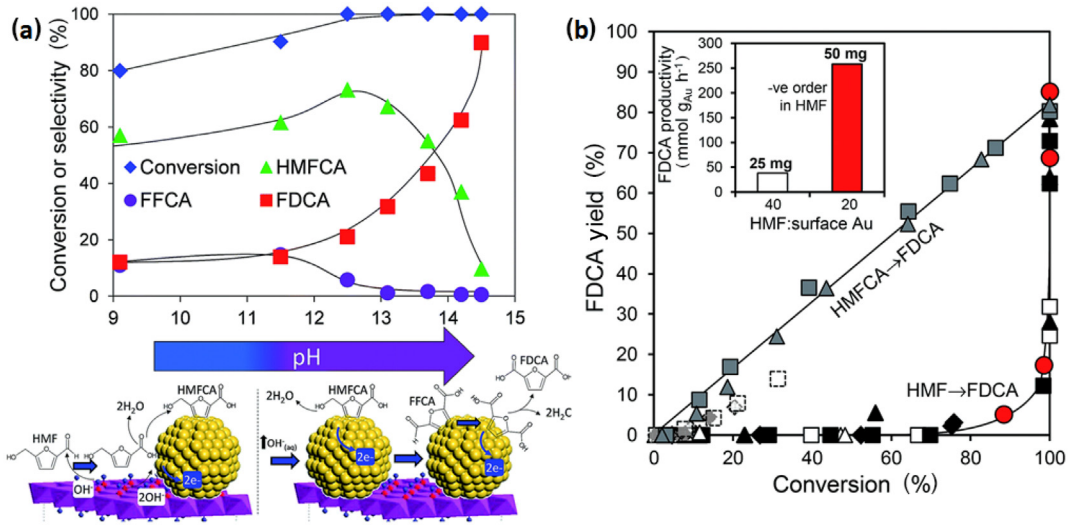


Fig. 6. (a) The pH dependence of HMF and intermediates oxidation. (b) The strong dependence of FDCA production on the concentration of reactively-formed HMFCA and surface Au sites [92]. Copyright 2015, The Royal Society of Chemistry.

aerobic oxidation of HMF in relatively low temperature (50 °C), in which needle-like CuO/Al_2O_3 exhibiting active and stable properties to achieve 98.6% yield of FDCA. The superior performance was attributed to the unique needle-like mullite structure and uniformly distributed CuO as active site. Zhang et al. [81] developed a highly active photocatalyst for HMF oxidation by immobilizing cobalt thioporphyrazine (CoPz) on graphitic carbon nitride (g-C_3N_4) to form CoPz/g-C_3N_4. Interesting, pure CoPz and CoPz/g-C_3N_4 catalysts were active to some extent in dark condition to show the same FDCA yield of 90% with the HMF conversions of 11.5% and 17.5%, respectively. CoPz was recognized as the active sites, whereas g-C_3N_4 was inactive for FDCA formation, whether there was light irradiation or not. Apart from the improved dispersion of CoPz by adding hydrophobic g-C_3N_4 support to provide more CoPz sites accessible to the polar substrate of HMF, the strong interaction between the CoPz and g-C_3N_4 resulted in a higher electronic cloud density in the CoPz/g-C_3N_4 than that in pure CoPz, and thus led to a much higher catalytic activity under the same conditions. Su et al. [82] compared the catalytic performance of Mo- and W-based heteropoly acids for HMF oxidation by H_2O_2 at 100 °C for 2 h. Quaternary ammonium dectungstate embraced an equal number of single epoxy groups and double epoxy groups in the presence of H_2O_2. The high steric hindrance of quaternary ammonium inhibited the HMFCA oxidation into FDCA since the double epoxy groups as the active sites were competitively adsorbed by a quaternary ammonium. However, three quarters of the double epoxy group in quaternary ammonium octamolybdate were free from quaternary ammonium, which endowed the Mo-based catalyst a superior activity to FDCA.

Leaching or leakage of metal ions from metal-based catalysts resulted in increased production cost and difficult product purification. Therefore, the development of efficient metal-free catalysts for the aerobic oxidation of HMF is appropriate for great significance. Nguyen and co-workers [83] reported the oxidation of HMF to FDCA using the zeolitic-imidazole framework (ZIF-8) derived nitrogen-doped nanoporous carbon (NNC) as the catalyst. Graphitic N (N-Q) in these NNC catalysts was recognized as the catalytic active sites due to the fact that the FDCA yield was proportional to the amount of N-Q, while there was no relationship between the activity and the amount of pyridinic-N or pyrrolic-N species. A similar role of N-Q was also reported in our previous work on oxidative dehydrogenation of propane by nitrogen-doped carbon nanotubes [84]. The full conversion of HMF was achieved within 4 h at 80 °C and ambient pressure when the yield of FDCA increased to a maximum of 80% with the reaction time. The reaction pathway on the doped carbon catalyst would be HMF-HMFCA-FFCA-FDCA due to the absence of DFF intermediate. The FFCA-FDCA step was the rate-determining step and the consumption of HMFCA or FFCA was relatively slow compared to HMF. Varma et al. [85] developed a porous nitrogen-enriched carbon nitride catalyst (PCN_x), via carbonization of marine waste originated from chitosan, for the aerial oxidation of HMF to FDCA under mild reaction conditions. The oxidation of HMF over PCN_x was accomplished in 83% FDCA yield under ambient pressure at 70 °C. The PCN_x catalyst exhibited good recyclability without any significant loss in its activity and structure for five runs. On account of the widely reported effect of graphitic nitrogen on oxygen activation in gaseous and liquid reactions, this study also compared nitrogen-doped graphene and graphitic carbon nitride (g-C_3N_4), obtaining only 5% and 15% yield of FDCA in the same conditions, respectively. Therefore, the conclusions that graphitic nitrogen in PCN_x activates O_2 and is critical to the aerobic oxidation of alcohols need more details to support. Anyway, green metal-free catalysts will play a more prominent role in the catalytic oxidation of biomass or other organic compounds if the number of active centers with a precise molecular structure could be greatly enhanced. The catalytic performance of HMF oxidation into FDCA over cheap metal and carbon-based catalysts are listed in Table 3.

2.2. Solid alkali system

2.2.1. Hydrotalcite and layered double hydroxide

The excess use of homogeneous bases is likely to cause equipment corrosion during the reaction and large energy consumption in the product isolation procedure, and thus a variety of recoverable solid bases have attracted increasing attention. Hydrotalcite (HT), one of the layered double hydroxides (LDHs) consisting of brucite-like layers with abundant –OH groups on the surface, emerged as a rising-star solid base material for dispersing metal NPs to prevent aggregation. However, HT is not stable enough at low values of pH (pH < 9.0) [86], which can be readily etched and neutralized by acidic reagents. Davis et al. [87] certified that the employment of HT to replace NaOH in the HMF reaction medium benefited the production of FDCA (>99% yield) over Au/TiO_2, but stoichiometrical consumption of magnesium ions triggered the severe leaching of HT by forming soluble salts of the product

diacid due to the high acidity of FDCA (pK_a = 2.28 ± 0.10) [88]. In order to slow the Mg dissolution, an excess HT added to the reaction to reach a higher pH throughout the reaction [87]. Similar to the liquid alkali oxidation, the final product diacid can also isolate from the product solution by filtering or centrifugation following by acidification. However, the separation of catalyst and the rest HT from each other raise additional difficulties if the HT is not completely consumed. Despite the consumption, Mg-Al HT can also be used as the additive to the Ru/AC catalyst to afford high efficient oxidation of HMF to FDCA, being superior to the bases like MgO, $Ca(OH)_2$, K_2CO_3 and NaOH on the basis of its proper strength of basicity [89,90]. Gupta et al. [91] directly employed HT as a basic support of gold nanoparticles to efficiently catalyze the HMF-FDCA reaction using molecular oxygen in water at 95 °C, where the basicity of HT assisted the conversion of aldehydes into hemiacetals as well the production of gold alcoholate species via gold hydride shift from HMFCA. Ardemani et al. [92] subsequently demonstrated that the moderate strength base sites of hydrotalcites and the high fraction of exposed gold atoms synergically contributed to selective cascade oxidation of aldehyde and alcohol (Fig. 6). Gorbanev et al. [93,94] observed that ruthenium hydroxide supported on HT and other metal oxides could afford FDCA with the highest yield of ~ 100% under optimized condition. However, ICP analysis confirmed that magnesium-based HT and oxide supports dissolved partially to leach Mg ions during the catalytic reaction. In 2016, basicity-tuned HT-supported Pd catalysts for the highly efficient oxidation of HMF to FDCA in aqueous solutions were reported [95]. The FDCA yield higher than 99.9% was achieved under mild conditions when the Mg/Al molar ratio of HT was 5, which could be attributed to the moderate basicity of the Mg-Al-CO_3 hydrotalcite and the sufficient –OH groups on the surface. Importantly, these catalysts could be recycled at least five times without apparent loss in the reaction reactivity. Monometallic and bimetallic Pt catalysts supported on HT were also systematically studied to understand the influence of metal species on catalytic activity [96,97]. Ebitani et al. demonstrated that the type of metals employed and their ratio of the combination were closely related to the activity of the catalysts, following the order of PdPt-PVP/HT > Pt-PVP/HT > AuPd-PVP/HT > Pd-PVP/HT > AuPt-PVP/HT > Au-PVP/HT. Among these catalysts, the bimetallic $Pd_{20}Pt_{80}$-PVP/HT owned the highest activity to produce FDCA (>99% yield) without the addition of a soluble base [96]. Interestingly, beyond the synergistic effect between Au and Pd supported on HT [57] and CaMgAl-LDH [98], Fang and his co-workers [99,100] revealed the synergy between two components in HT-activated carbon composite (HT-AC) support. As comparing to Au/HT and Au/AC catalysts, the co-presence of HT and activated carbon (AC) in the support of Au/HT-AC with the optimal mass ratio (2:1) would significantly enhance the catalytic activity and stability.

2.2.2. Other basic supports or additives

In addition to HT and LDH, some novel basic supports have been reported recently. Cho et al. [101] investigated a series of basic metal oxide supported Ru catalysts and found the catalytic activity for HMF oxidation was related primarily to the basicity of support in the order of MgAlO > MgO > ZrO_2 > CeO_2 ≫ La_2O_3. Unexpectedly, the most active MgAlO support was not stable under the catalytic condition and seriously dissolved due to the poor resistance to the acidic nature of the produced FDCA. However, Ru/MgO, a bit less active than Ru/MgAlO, afforded a 100% conversion of HMF with greater than 90% yield of FDCA at 160 °C in 4 h and could be reused 5 cycles without a significant loss in activity. Wang et al. [102]

Table 4
Catalytic performance of HMF oxidation into FDCA in solid base system.

Catalysts	HMF	T[a]	t[b]	Solvent	Oxidant[c]	Conversion[d]	Yield	Reaction rate		Ref.
	(mM)	(°C)	(h)			(%)	(%)	(mmol g_{cat}^{-1} h^{-1})		
								HMF	FDCA	
Au/TiO_2	166.7	90	20	HT in H_2O	0.34 MPa O_2	100	99	0.609	0.603	[87]
Ru/C	100	150	12	HT in H_2O	2 MPa O_2	100	78.2	1.938	1.516	[89]
commercial Ru/C	100	120	5	1 equiv. HT	0.2 MPa O_2	100	90	2.000	1.800	[90]
Au/HT	166.7	95	7	H_2O	0.1 MPa O_2	99	99	0.551	0.551	[91]
$Ru(OH)_x$/HT	50	140	6	H_2O	0.25 MPa O_2	100	100	0.794	0.794	[93]
$Ru(OH)_x$/MgO	50	140	20	H_2O	0.25 MPa O_2	100	100	0.238	0.238	
$Ru(OH)_x$/MgO	50	140	6	H_2O	0.25 MPa O_2	100	93	0.792	0.736	[94]
$Ru(OH)_x$/MgO·La_2O_3	50	140	6	H_2O	0.25 MPa O_2	100	100	0.792	0.792	
1% Pd/HT-5	40	100	7	H_2O	0.1 MPa O_2	99	91.3	0.566	0.522	[95]
2% Pd/HT-5	40	100	3	H_2O	0.1 MPa O_2	99.4	92.4	1.325	1.232	
2% Pd/HT-6	40	100	8	H_2O	0.1 MPa O_2	99.9	99.9	0.500	0.500	
PdPt-PVP/HT	100	95	11.5	H_2O	0.1 MPa O_2	100	99	0.621	0.615	[96]
4.9 wt% Pt/HT	25	95	14	H_2O	0.5 MPa O_2	100	97	1.794	1.741	[97]
Au-Pd(1:1)/HT	25	100	12	H_2O	0.5 MPa O_2	100	91	0.527	0.480	[57]
Au-Pd(1:1)/MgO	25	100	12	H_2O	0.5 MPa O_2	100	99	0.522	0.517	
AuPd/CaMgAl-LDH	12.5	100	6	H_2O	0.5 MPa O_2	96.1	89.4	1.570	1.408	[98]
AuPd/La-CaMgAl-LDH	12.5	100	6	H_2O	0.5 MPa O_2	96.1	89.4	1.602	1.490	
1% Au/HT-AC(2:1)	25	100	12	H_2O	0.5 MPa O_2	100	99	0.423	0.417	[99–100]
Ru/MgAlO	100	140	4	H_2O	0.62 MPa O_2	100	99	2.500	2.475	[101]
Ru/MgO	100	140	4	H_2O	0.62 MPa O_2	88	58	2.200	1.45	
Pt/C-O-Mg	50	110	12	H_2O	1 MPa O_2	100	97	1.042	1.010	[102]
Pt/C-EDA-4.1	50	110	12	H_2O	1 MPa O_2	99	96	1.031	1.000	[103]
Pt/NC-CeO_2	12.5	150	4	H_2O	0.4 MPa O_2	100	99.9	1.250	1.249	[104]
Pt/C_3N_4	12.5	150	4	H_2O	0.4 MPa O_2	71.9	18.1	0.899	0.226	
Pt/CeO_2	12.5	150	4	H_2O	0.4 MPa O_2	97.8	71	1.223	0.888	
AuPd-*n*NiO	20	90	6	H_2O	1 MPa O_2	95	70	0.985	0.726	[105]
Ru/CTF-c	66.7	140	1	H_2O	2 MPa Air	99.9	41.4	19.98	8.28	[20]
Fe^{III}-POP-1	158	100	10	H_2O	1 MPa Air	100	79	26.33	20.80	[6]

[a] reaction temperature
[b] reaction time
[c] reaction oxidant and pressure
[d] conversion of HMF

designed a novel Pt/C-O-Mg catalyst by encapsulating MgO particles in carbon and then loading platinum on the carbon surface. The Pt/C-O-Mg catalyst exhibited satisfactory selectivity and stability due to the formation of C-O-Mg bond with the capability to create stable basic sites. Under the optimal conditions (110 °C, 1.0 MPa O_2), FDCA yield over this catalyst reached 97% and stabilized at around 95% with little deactivation after ten cycles. N-doped carbon supported Pt catalyst was also tested by this research group [103]. CO_2-TPD revealed that the doped nitrogen introduced a new moderate strength basic site on the carbon surface. The relationship between the catalytic activity and the relative abundance of nitrogen species suggested that the pyridine-type nitrogen species coordinated the HMF oxidation into FDCA. Moreover, increase of nitrogen content in carbon support has a promotion effect on catalytic activity by more basic sites and higher alkalinity. Li et al. [104] developed nitrogen-doped-carbon-decorated CeO_2 (NC-CeO_2) as a basic support to fabricate Pt/NC-CeO_2 catalyst, exhibiting exceptional catalytic efficiency superior to the Pt catalysts supported on CeO_2 and g-C_3N_4 with an almost 100% FDCA yield at 110 °C for 8 h (or 150 °C for 4 h) in free of any soluble base. CO_2-TPD demonstrated that the introduction of the electron-rich nitrogen atoms can strengthen the surface basicity, particularly a small amount of the strong Lewis base sites (SLB) on Pt/NC-CeO_2, which played an important role in improving the oxidation of –OH of HMF. Recently, nanosized NiO was also recognized to be an effective basic support to promote the HMF conversion. Albonetti et al. [105] interpreted the synergistic effect between AuPd alloy and NiO as the electronic and geometrical properties of AuPd metal were tuned by the NiO support, thereby affecting the substrate binding at the metal/support interface.

Besides the above inorganic base support, some nitrogen-containing organic materials were applied as basic support for heterogeneous catalysts due to their sufficient thermal stability and robust structure, as well as insoluble in most conventional solvents, acids, and bases. Artz et al. [20] reported that Ru clusters

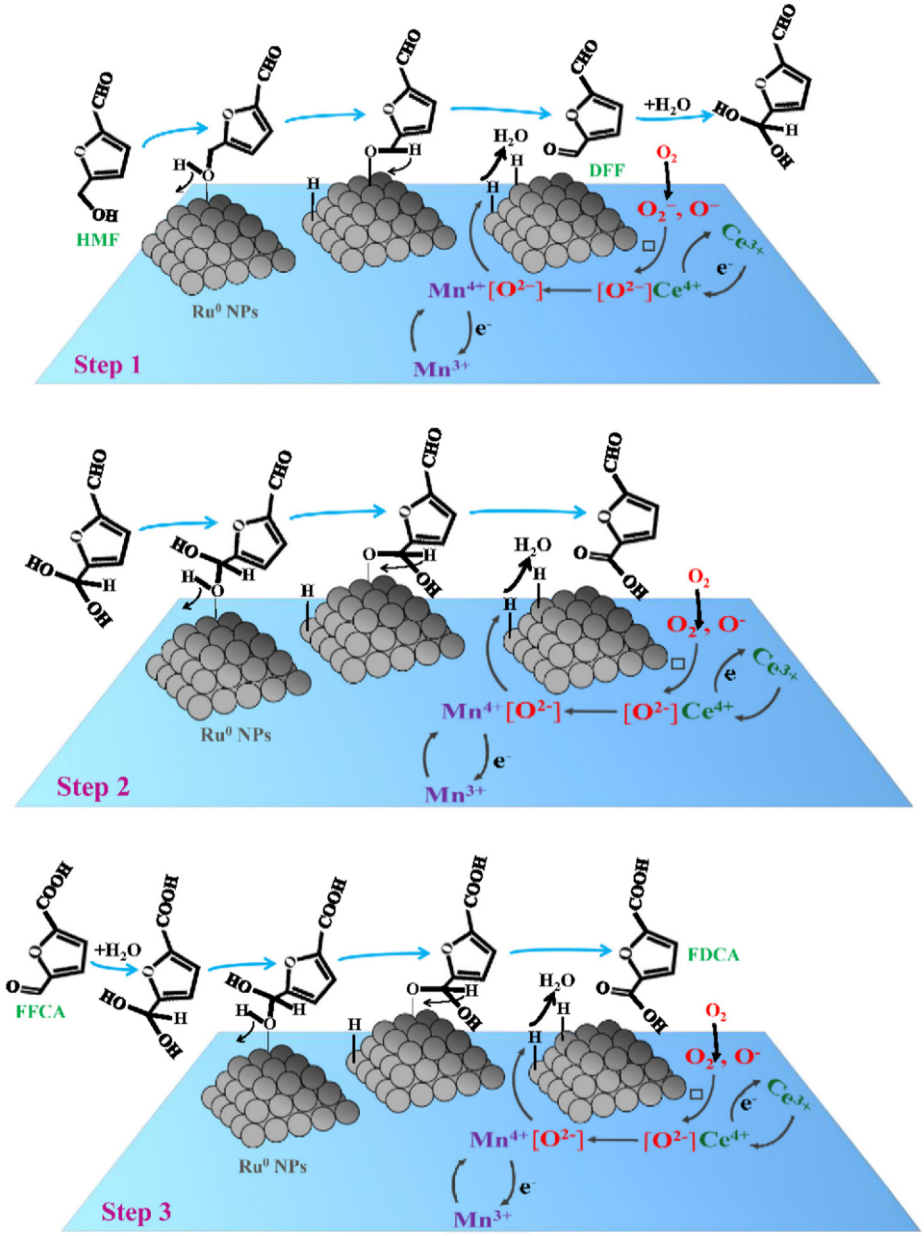


Fig. 7. Possible activation of HMF and oxygen to produce FDCA over the Ru/$Mn_xCe_1O_y$ catalyst [118]. Copyright 2018, Elsevier.

supported on covalent triazine frameworks (CTFs) provided a superior FDCA yield (91%) at 140 °C and 2 MPa of synthetic air without additional base. It was clarified that the hydrophilic carrier with a nitrogen content of 10.4% allowed the efficient oxidation of HMF to FDCA under the aqueous-phase conditions without any alkali additives. Saha et al. [6] introduced porphyrin-based porous organic polymer to loading Fe catalyst (Fe^{III}-POP-1) for the oxidation reaction to acquire a yield of FDCA up to 79% in 10 h under milder conditions. EPR spectra analysis of the recovered catalyst and the contrast experiment using homogeneous Fe^{III}–porphyrin complex as catalyst revealed that, the high surface area and Fe^{3+} as active sites of the Fe^{III}-POP-1 catalyst played a vital role for HMF oxidation. The Fe(III) mediated HMF oxidation was believed to undergo a radical chain mechanism involving a classical Fenton-type reaction and the formation of peroxyl radicals via thermal autoxidation. Even more significantly, this catalytic system did not need the use of soluble base and precious metal to afford full HMF conversion and a high FDCA yield, further inspiring the development of cheap and efficient catalysts for sustainable chemistry. Table 4 summarizes the catalytic performance of HMF oxidation using solid base system.

2.3. Base-free system

Generally, the oxidation of HMF in the basic environments is kinetically favorable and offers higher FDCA productivity, as seen in Fig. 2(b). However, the neutralization of the product solution and acidification of salt to diacid are essential and easy to produce wastes. Additionally, solid base supports can circumvent the requirement for liquid alkali additives for the oxidation of HMF, but the acidic nature of the generated FDCA has the potential to etch basic support and raise concerns on catalyst stability. Never-

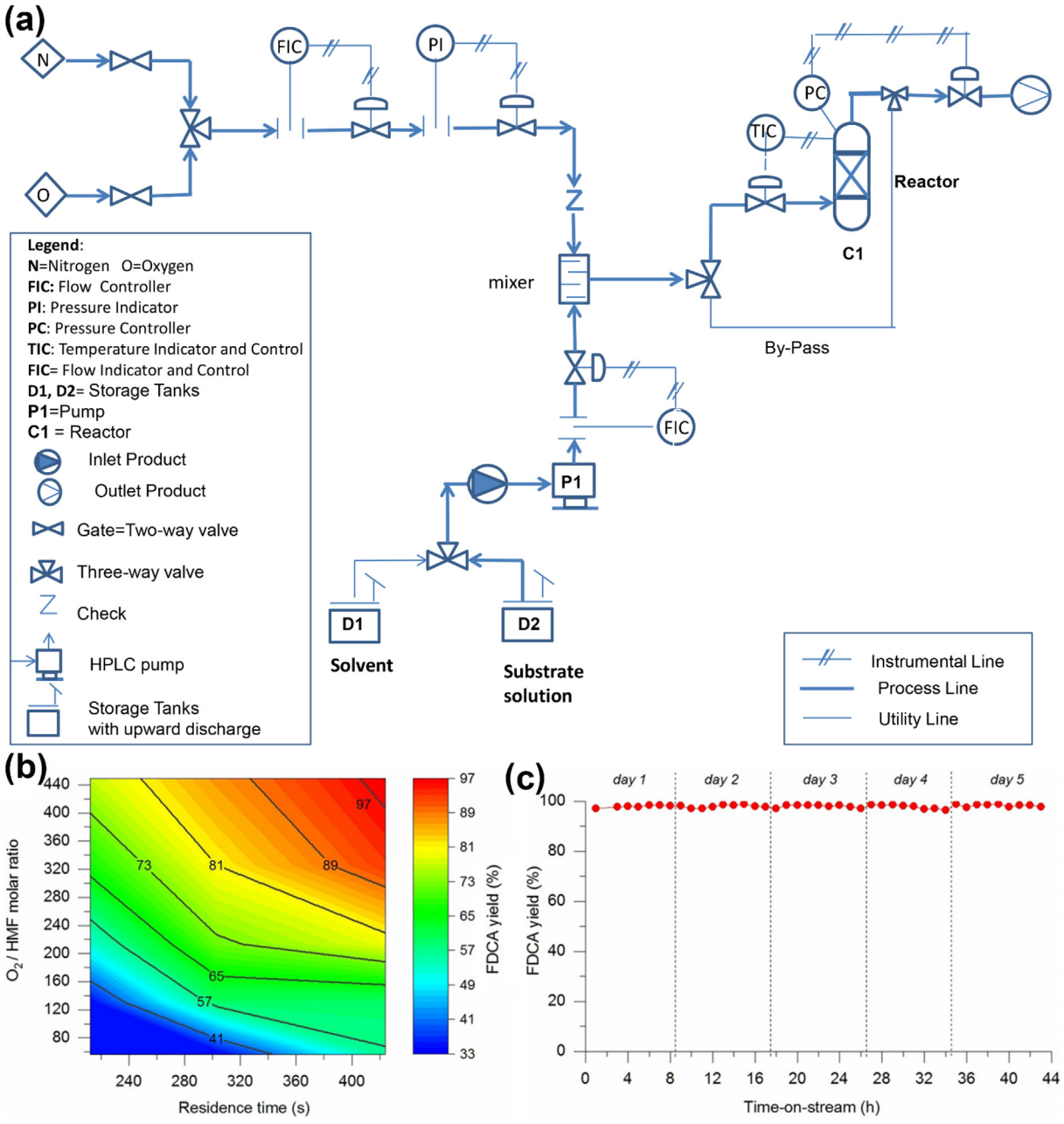


Fig. 8. The continuous-flow oxidation of HMF to FDCA over Pt@Dowex-Na catalyst [125]. (a) Schematic of the reactor system, (b) catalytic performance and (c) durability. Copyright 2019, Wiley-VCH Verlag GmbH & Co. KGaA, Weinheim.

theless, several heterogeneous catalysts under base-free conditions are challenging the previous base-participated researches, and they offer us hope to explore a completely sustainable process for FDCA production. In particular, noble metals owing to their outstanding role in the activation of oxygen show good catalytic ability in oxidizing –OH and –CHO groups to form corresponding aldehydes and acids. Combined with the intrinsical instability of HMF, the selective transformation to FDCA on noble metal become feasible even without the assistance of alkali additives. The base-free aerobic oxidation often follows a DFF-mediated pathway and the mechanism presented in Fig. 14, different from the situation using alkaline medium or solid base [3]. Overall, the base-free method is more simplified and environmental-friendly, despite the lower concentration of the feedstock and higher reaction temperatures are needed to drive the system to obtain moderate productivity of FDCA compared to the oxidations in alkaline medium (Fig. 2b). For the catalyst, the acidic-basic and adsorption–desorption properties of support have significant impacts on the catalytic behavior. Thanks to their extraordinary properties, such as high surface area, hierarchically porous structure, versatile surface chemistry, superior mechanical stability, as well as outstanding thermal and electrical conductivity, carbon materials proved to be outstanding support for the metal catalysts or used as high-performance catalyst directly [106,107]. Sharma et al. [108] found the HNO_3-refluxed carbon nanotube (CNT) enabled 86.5% HMF to convert totally into FFCA in base-free water, without any detectable FDCA, DFF, and other species, suggesting the catalytic ability of the functionalized CNT itself. After supported metals (Pt, Pd, Ru, Co, and Ni), the noble metal-loaded CNT catalysts showed high selectivity towards FDCA in the order of Pt/CNT > Pd/CNT > Ru/CNT, while the non-noble metal catalysts were more selective towards DFF. Wang and co-workers [57,97] previously showed that functionalized CNT supported Pt nanoparticles and Au-Pd alloy are able to catalyze the aerobic oxidation of HMF into FDCA with a high efficiency in water without any bases. The carboxyl groups on CNT surfaces pretreated by HNO_3 were unfavorable for the conversion of HMF to FDCA, whereas the carbonyl/quinone and/or phenol groups on CNT surfaces pretreated by H_2O_2 essentially enhanced the FDCA yield. This reaction turnover is quite similar to the previous work on the carbon-catalyzed selective oxidation of acrolein to acrylic acid by Frank et al., which revealed the determining role of carbonyl/quinone groups for oxygen insertion in acrolein molecules by reaction kinetics and in-situ XPS characterization [109]. Apart from CNT, graphene oxide (GO), reduced graphene oxide (rGO) [42], carbon nanofiber (CNF), activated carbon (AC) [90] and carbon black [110] were also applicable to support noble metal nanoparticles to catalyze this reaction to some extent, while SiO_2, Al_2O_3, TiO_2, ZrO_2, and CeO_2 supported catalysts were inactive under the base-free condition in Wang's system [57,97]. However, these oxides were often reported to support catalyst to realize remarkable activity for FDCA production [111,112]. For instance, Pt catalyst supported on low surface area ZrO_2 using atomic layer deposition (ALD) showed a high activity close to the aforementioned Pt/CNT catalyst in terms of turnover frequency (TOF) under similar conditions, i.e., 6.85 h^{-1} vs. 7.00 h^{-1}. This was mainly ascribed to the high Pt dispersion and uniform active sites as well as the desirable adsorption ability of the reactant/intermediates achieved by ALD technique [113,114]. Similar strategy for increasing dispersion was employed by Pichler et al. [115] to establish a high-surface-area ZrO_2 supported Ru catalyst to realize a full conversion of HMF with 97% yield of FDCA, suggesting once again the influence of support properties derived from different synthesis method on metal particle size and consequent catalytic activity.

Prompted by the diverse chemical states and specific oxidative properties, as discussed in 2.1.3 section, Mn-containing catalysts exhibit remarkable catalytic performance for HMF oxidation even without the aid of base additives. Kim et al. [116] developed a new class of Mn-Co-O spinel supported Ru catalysts with a pronounced yield of FDCA (99.1%) and good recyclability in a pure water solvent, and they attributed the reason to the coexistence of Lewis and Brønsted acidic sites. Actually, such a solid support can be seen as a heterogeneous replica of homogeneous Co$(OAc)_2$/Mn$(OAc)_2$/HBr for HMF oxidation, likely going through a similar redox cascade [117]. Mn-Ce mixed oxides-supported Ru NPs ($Ru/Mn_XCe_1O_Y$) were firstly employed by Gao et al. [118] as a base-free catalyst for HMF oxidation, undergoing a DFF-intermediated reaction route to yield the final product FDCA. Ru^0 species were believed to adsorb and activate HMF, while the mixed oxides- support facilitated the adsorption, dissociation, and mobility of oxygen (Fig. 7). The authors announced that the strong metal-support interaction together with the synergy between Ce and Mn oxides highly contributed to the superior performance of $Ru/Mn_6Ce_1O_Y$, exhibiting a high catalytic activity with 95% FDCA yield (TOF = 5.3 h^{-1}) and excellent stability after 8 runs. Taking the strong redox properties of MnO_2 and CuO into consideration, Ventura et al. [119] directly utilized quaternary $CuO{\cdot}MnO_2{\cdot}CeO_2$ oxide as a catalyst to convert HMF into FDCA under aqueous phase with O_2 as oxidant, demonstrating the independence of external bases and precious metals to maintain a considerable activity with high stability after 12 runs. Although the yield of product was limited at 70.8% due to the deposition of humins or organics on the catalyst, supplementing fresh catalyst or decarbonizing spent catalyst could eliminate the limitation to achieve much higher FDCA yield up to 98.7%. Simple calcination at 550 °C could recover the catalytic activity by not only excluding carbon deposit but also repairing the transient deactivation derived from Cu^{2+} reduction to Cu^0 rather than leaching. This inspires us for more efforts in developing appropriate catalyst to resist carbon deposition. More importantly, the acidic/basic properties of the mixed oxides can be moderated by varying the calcination temperature, showing the possibility to regulate the distribution of products in pure water as solution [120–122]. The similar tunable acidic-basic properties also exist in hydroxyapatite (HAP) materials and rely critically on its Ca/P ratio, showing both the acidic and basic characteristics when the Ca/P ratio among 1.50 to 1.67. For the base-free aerobic catalysis on Ru/HAP, besides the critical role of Ru, the basic sites of support acted to cleave the O–H bond of HMF to form a Ru-alkoxide intermediate and promote the subsequent oxidation of –CHO to –COOH, while the acidic sites of support involved in oxidizing the Ru hydride to generate a H_2O molecule [123].

Adoption of pure water as a solvent without any basic or acidic additives has been an important direction for this reaction. However, the limitations still exist to some extent in base-free system, such as unsatisfactory activity of catalysts, leaching of active components by the strong acidity of product, side reactions under the harsh reaction conditions, coverage of catalytic sites by FDCA deposition, as well as the low productivity and sustainability by batch reaction. Performing base-free aerobic oxidation in continuous mode will fix some of the shortcomings. In 2010, Lilga et al. [124] first reported HMF oxidation in a bench-scale flow reactor with aqueous HMF feed under basic, neutral, and acidic conditions. A 3/8-inch stainless-steel tube heated in a tube furnace was employed as a fixed-bed reactor to screen catalysts and operating conditions. As a result, during the two-week neutral continuous-flow reaction, the aerial oxidation over 5% Pt/ZrO_2 catalysts steadily afforded full HMF conversion with FDCA yield of up to 98% at 100 °C with a 0.5 wt% HMF feed (liquid hourly space velocity = 3 h^{-1}), in spite of inhibition occurring by precipitate. Recently, Liguori et al. [125] exploited a continuous-flow production of FDCA in neat water using Pt nanoparticles immobilized on sulfonated DOWEX 50WX2-100 cation-exchange resin (Pt@Dowex-Na) as a

Table 5
Catalytic performance of HMF oxidation into FDCA in base-free system.

Catalysts	HMF	T[a]	t[b]	Solvent	Oxidant[c]	Conversion[d]	Yield	Reaction rate		Ref.
	(mM)	(°C)	(h)			(%)	(%)	(mmol g_{cat}^{-1} h^{-1})		
								HMF	FDCA	
Pt/rGO	25	95	16	H_2O	0.5 MPa O_2	100	99	1.603	1.587	[42]
Pt/Fe_3O_4/rGO	25	95	9	H_2O	0.5 MPa O_2	100	99	2.849	2.821	
commercial Ru/C	100	120	10	H_2O	0.2 MPa O_2	100	88	0.500	0.440	[90]
4.9 wt% Pt/CNT	25	95	14	H_2O	0.5 MPa O_2	100	98	1.794	1.758	[97]
4.9 wt% Pt/GO	25	95	14	H_2O	0.5 MPa O_2	100	95	1.794	1.704	
Au-Pd(1:1)/CNT	25	100	12	H_2O	0.5 MPa O_2	100	94	0.527	0.496	[57]
Pt/CNT	NA[e]	100	12	H_2O	3 MPa O_2	100	97.8	0.008	0.008	[108]
Pd/CNT	NA[e]	100	12	H_2O	3 MPa O_2	100	95.6	0.015	0.015	
Ru/CNT	NA[e]	100	12	H_2O	3 MPa O_2	100	92.8	0.015	0.014	
Pt/C-30	100	105	6	H_2O	0.5 MPa O_2	100	63	4.990	3.144	[110]
Pt_1Sn_1-H_2/TiO_2	NA[e]	110	4	H_2O	1.0 MPa O_2	68	13	1.084	0.207	[112]
Pt/ZrO_2-ALD-30	39.7	100	12	H_2O	0.4 MPa O_2	100	97.3	0.992	0.965	[113]
50Pt-Ni/AC	39.7	100	6	H_2O	0.4 MPa O_2	100	43.1	1.984	0.855	[114]
$Ru/ZrO_{2\ H\text{-}aero}$	50	120	16	H_2O	0.1 MPa O_2	100	97	0.947	0.919	[115]
$Ru/MnCo_2O_4$	100	120	10	H_2O	2.4 MPa air	100	99.1	1.331	1.319	[116]
Ru/MnO_2	100	120	10	H_2O	2.4 MPa air	98.8	31.1	1.315	0.414	
Ru/CoO	100	120	10	H_2O	2.4 MPa air	91.1	17.8	1.212	0.237	
$Ru/Mn_6Ce_1O_Y$	100	150	15	H_2O	1.0 MPa O_2	100	99.9	0.739	0.739	[118]
$Ru/Mn_6Ce_1O_Y$	100	120	18	H_2O	1.0 MPa O_2	100	95	0.385	0.366	
Ru/Mn_3O_4	100	120	18	H_2O	1.0 MPa O_2	96	58	0.370	0.223	
Ru/CeO_2	100	120	18	H_2O	1.0 MPa O_2	44	12	0.169	0.046	
$CuO{\cdot}MnO_2{\cdot}CeO_2$	15	130	12	H_2O	0.9 MPa O_2	97.4	71	0.170	0.124	[119]
Ru/HAP	100	120	24	H_2O	1 MPa O_2	100	99.6	0.155	0.154	[123]
Pt/ZrO_2[f]	39.9	100	NA[e]	H_2O	1.03 MPa air	100	98	-	-	[124]
Pt@Dowex-Na[g]	25	120	22	H_2O	2 MPa O_2	100	98	2.273	2.227	[125]
Pt@Dowex-Na[f]	25	120	8	H_2O	0.77 MPa O_2	100	99	1.750	1.740	

[a] reaction temperature
[b] reaction time
[c] reaction oxidant and pressure
[d] conversion of HMF
[e] not available
[f] continuous-flow reaction
[g] batch reaction

catalyst, realizing productivity of 1.74 mmol $g_{cat}^{-1}h^{-1}$ in 99% yield at 120 °C and 0.77 MPa O_2 with 303 s residence time. The home-made continuous-flow system, composing mainly of a catalyst loaded glass tube reactor (I.D = 3 mm, L = 50 mm) and a controlled feeding apparatus, could afford a space–time-yield of 46 g_{FDCA} L^{-1} h^{-1} in 99% purity after water withdrawal (Fig. 8). Although there are few reports so far, base-free continuous-flow production of FDCA is of great significance for developing more sustainable technology for biomass conversion and utilization. Table 5 summarizes the catalytic performance of HMF oxidation into FDCA in base-free systems.

3. Electrochemical oxidation of HMF

Electrochemical catalysis has been considered as an alternative to the thermocatalysis, employing the electrode potential rather

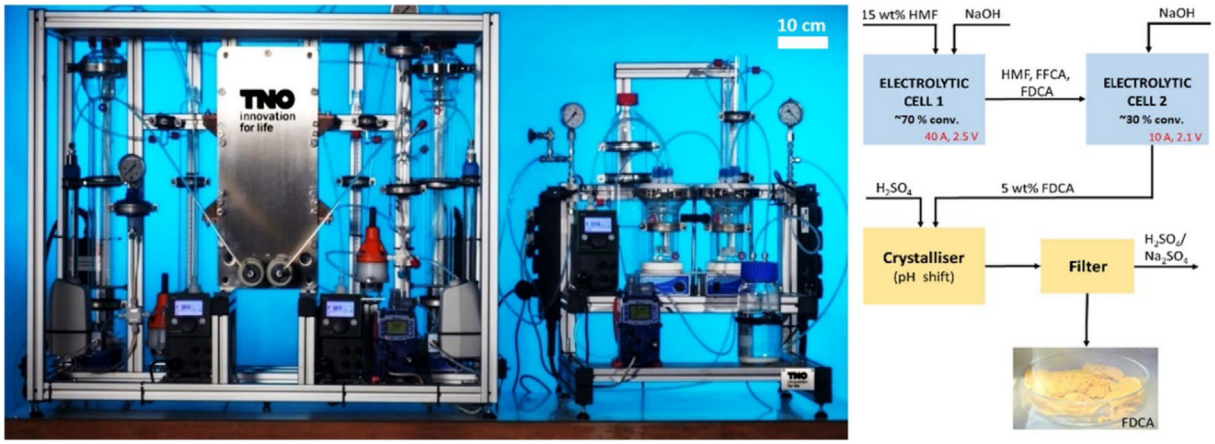


Fig. 9. (left) Bench-scale continuous setup and (right) the process diagram for FDCA production and separation [145]. Copyright 2018, Springer Nature.

than chemical potential as the main driving force. Beyond the regulation of substrates concentration and reaction temperature or pressure in the traditional heterogeneous and homogeneous catalysis, the management of electrochemical reaction parameters realizes more accurately and conveniently by controlling the electrode potential and circuit current [126,127]. In addition, compared to the aerobic thermocatalysis, electrooxidation is a promising technology with many significant characteristics, such as extensive substrate tolerance, mild reaction conditions, low energy dissipation, high atom economy, as well as superior safety (no additional oxygen is required). In the past few decades, the electrocatalytic oxidation had made considerable progress in the fields of organic synthesis [128], pollutant degradation [129], and energy conversion [130]. To our knowledge, the first study on electrolysis of HMF was reported by Kawana et al. in 1983 [131], while electrooxidation of HMF into FDCA was first reported by Grabowski et al. in 1991 [132]. However, this research field had been scarcely progressed in the following score years since then, possibly due to the indifference of biomass by the academic and industry researchers. Until recent years, HMF electrooxidation has drawn growing attention, involving the design of electrocatalyst, coupling of reactions and the possible pathway.

3.1. Electrochemical oxidation by supported noble metal catalysts

Similar to most of the heterogeneous catalysis, the electrocatalytic process often involves a surface reaction process at the interface between the active electrode and electrified electrolyte. Therefore, some thermochemically active catalysts, such as precious metals and their corresponding supported catalysts, have been proved to be electrochemically active in the same or similar reaction. In 2012, Strasser and Vuyyuru employed pure Pt foil as a working electrode for HMF oxidation in a NaOH-$NaClO_4$ aqueous solution (pH = 10). The electrochemical activation of water in anode resulted in the in-situ generation of reactive oxygenated species and thus eliminated the need of molecular oxygen to oxidize HMF. The electrocatalytic oxidation of HMF was found very selective to form 18% yield of DFF with 70% conversion of HMF within 12 h, showing a quite different product distribution from that of heterogeneous process catalyzed by Pt/C in the same pH environment [23]. Zhou et al. [42] recently found the oxidation peak potentials of –OH and –CHO of HMF on both Pt/Fe_3O_4/rGO and Pt/rGO catalysts were centered at 0.5 and 0.9 V vs Ag/AgCl, respectively. By using furfuryl alcohol and furfural as simplified substrates, the further electro-oxidation revealed that the oxidation peak potential for the first substrate (0.85 V) was lower than the second substrate (0.92 V), demonstrating that the oxidation of −OH to −CHO is prior than that of −CHO to –COOH in neutral K_2SO_4 electrolyte. In addition, the intermediate products were detected to be DFF and FFCA after reaction in a neutral electrolyte, while only HMFCA could be detected when using 0.1 M KOH as an electrolyte. On the other hand, in 2014, Li and co-workers [63] reported the product distribution of HMF oxidation in the anion-exchange membrane electrolysis flow cell, was highly dependent on the electrode potential and catalyst surface composition. On Au/C catalyst, the oxidation of –CHO was greatly favored over oxidation of –OH to generate HMFCA, while higher electrode potentials were required for further oxidation of the –OH to yield the final FDCA. However, for the Pd/C catalyst, HMF oxidation followed two competitive routes to form FDCA and the pathway relied on the electrode potential. Furthermore, at the low potential region, oxidation of –CHO over Pd/C was much slower than that over Au/C, but was greatly enhanced by increasing potentials or alloying with Au. The Pd–Au bimetallic catalysts (Pd_2Au_1/C and Pd_1Au_2/C) achieved much higher FDCA yield at lower potentials than the two monometallic catalysts. This observation provided promising strategies to adjust the reaction pathway and depth of HMF electrochemical oxidation by altering the surface composition of catalyst and regulating the applied potential.

3.2. Electrochemical oxidation by transition metal catalysts

Driven by the electrochemical potential, more and more innovative and cheap catalysts developed from earth-abundant transition metals, such as Ni_2P [133], CoP [134], Ni_2S_3 [135], porous Ni [136], Ni_xB [137], CoB [138], NiB_x [139], $NiCo_2O_4$ [140,141], VN [142], Ni_3N@C [143], Ni/Co/Fe oxyhydroxides [144], Ni/NiOOH [145], nanocrystalline Cu foam [146], $CuNi(OH)_2$/C [147], NiSe@NiO_x [148], NiFe-LDH [127], and Cu_xS@NiCo-LDH [149], were reported to be more efficient than noble metal catalysts, reversing the situation that the precious metal catalysts are more active and popular than the transition metal catalysts in HMF thermocatalytic oxidation. Grabowski et al. [132] firstly reported the HMF electrooxidation into FDCA on NiOOH anode, realizing 71% FDCA yield with 84% faradaic efficiency (FE) in a divided H-shape electrolyzer with 1 M NaOH aqueous electrolyte. By applying the similar Ni/NiOOH foam as electrodes, Latsuzbaia et al. [145] successfully realized the continuous production of FDCA from HMF in an industrial type plate-and-frame electrolyzer with integrated product separation system for the first time (Fig. 9). Although the continuous HMF oxidation was performed in two steps, an unprecedented FDCA separation yield of up to 95% was obtained within the bench-scale setup [145]. Also in 2018, Han and co-workers [140] observed the significant improvement in the catalytic kinetics by introducing Co into electrocatalysts, as well as the synergetic effect of Ni and Co species in charge transfer kinetics. With the optimal doping level, the hydrothermal grown $NiCo_2O_4$ nanowires on Ni foam required only 1.55 V vs. RHE to maintain the maximum oxidation of HMF and the minimum water oxidation. By passing the stoichiometric amount of charge (35C), $NiCo_2O_4$ nanowires exhibited the best performance of up to 90% FDCA yield with 99% FE, and preserved robust structural stability after five catalytic cycles. Further XPS and XANEX analysis by Kang et al. [141] revealed that the reason for the increased HMF oxidation efficiency of $NiCo_2O_4$ was the higher portion of reduced Co^{3+} to Co^{2+} under applied potential in $NiCo_2O_4$ electrode than Co_3O_4 electrode. In view of the actual catalytically active species of transition metal-based electrocatalysts are most likely oxyhydroxide phases in an alkaline electrolyte, the intrinsic catalytic properties of oxyhydroxides for HMF oxidation is a pressing topic to investigate systematically. Recently, Chio et al. [144] comparatively studied the catalytic activity of electrochemically prepared MOOH films (M = Ni, Co, and Fe) on the FTO substrate for the electrochemical oxidation of HMF into FDCA using a three-electrode setup with 0.1 M KOH electrolyte. The investigation pointed out that NiOOH is the most active catalyst to achieve up to 96.0% FDCA yield and FE at 1.47 V vs RHE. HMF oxidation rate could be further increased by applying more positive potential, however, the FDCA yield and FE would decrease as the competitive water oxidation became an increasingly dominant reaction. Despite of the fact that CoOOH has the ability to initiate HMF oxidation at a less positive potential than NiOOH due to the Co^{2+}/Co^{3+} conversion occurring at a less positive potential, the $Co(OH)_2$/CoOOH mediated HMF oxidation under constant potential was less efficient than $Ni(OH)_2$/NiOOH-mediated HMF oxidation due to the slower kinetics and the fact that not all Co^{3+} sites in CoOOH could be used for the reversible catalytic cycles. Among the three catalysts, FeOOH films were not efficient for HMF oxidation as they did not exhibit any activity for HMF electrooxidation at potentials prior to water oxidation while only trace amounts of DFF, HMFCA, FFCA, and FDCA could be detected during constant potential HMF oxidation performed at 1.71 V. This observation also obtained the effect of the film thickness on the current generated by different

oxidation pathways, contributing to a better understanding of the catalytic active sites and mechanisms of HMF oxidation on transition metal electrocatalysts in the alkaline system. For the sake of further reduction of the operating cost in product separation, electrochemical oxidation of HMF in acidic media was also explored by the same research group to enable FDCA spontaneous precipitation, due to the fact that FDCA precipitates out when the pH is below < 2–3 [150]. As a catalyst being highly stable in strong acid media under anodic bias and prefer HMF oxidation to water oxidation, the MnO_x anode could oxidize both the –OH and –CHO groups of HMF to achieve 99% HMF conversion and 53.8% FDCA yield in a pH 1 H_2SO_4 solution by applying a potential of 1.6 V vs. RHE, whereas Pt electrode as contrast could oxidize the –OH group to generate DFF but was unable to catalyze the further oxidation to

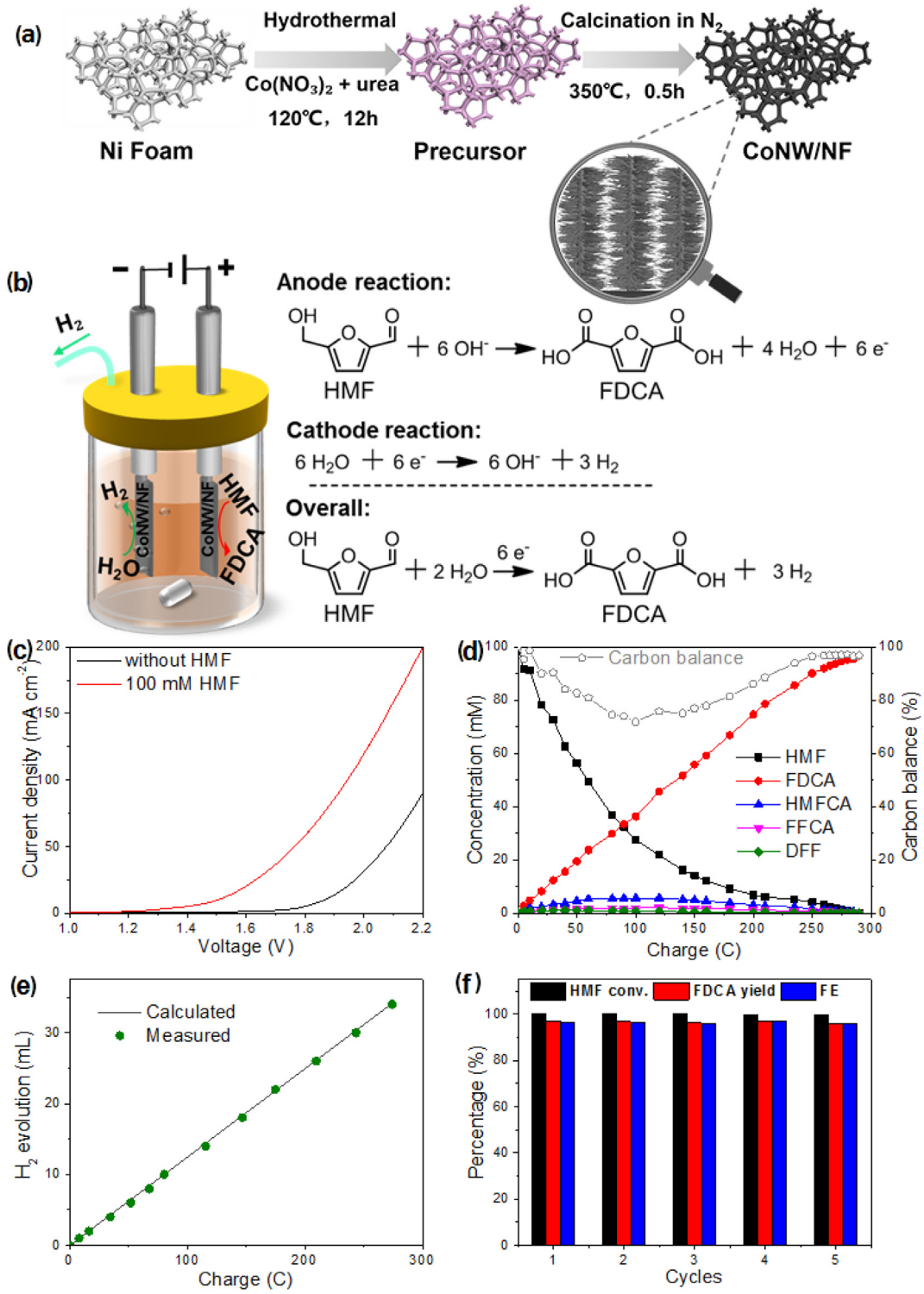


Fig. 10. The bifunctional CoNW/NF catalysts for simultaneous production of FDCA and hydrogen [153]. Schematic diagrams of (a) the fabrication of Co_3O_4 nanowires on nickel foam and (b) the integrated reaction. (c) LSV curves with and without HMF, (d) product quantitative analysis of chronoamperometric HMF oxidation, (e) theoretical and practical H_2 release, (f) durability investigation. Copyright 2019, The Royal Society of Chemistry.

FDCA even at 2.0 V vs. RHE. One of the disadvantages of using acidic media is FDCA spontaneously precipitated out on the electrode surface during electrolysis, thereby hindering further electrochemical oxidation. The downside can be addressed by elevating reaction temperature to 60 °C to improve the solubility of FDCA, therefore a simple but efficient separation method was developed accordingly by altering the temperature instead of the solution pH. Another drawback of acidic electrolysis is the limited product selectivity due to the formation of about 20% yield of maleic acid, in spite of which is another biomass-derived platform molecule with wide industrial applications [150].

The promising ability to upgrade HMF into value-added chemicals in mild conditions by electrochemical oxidation instead of aerobic oxidation is already quite attractive, while more benefits arise when considering the integration of the anodic oxidation and cathodic reduction reactions. By coupling HMF oxidation to cathodic hydrogen evolution reaction (HER) in a single electrolyzer, the integrated system can achieve higher utilization efficiency of input energy due to the more favorable thermodynamics of HMF oxidation than that of oxygen evolution reaction (OER) in water. In addition, the bio-based products are undoubtedly more valuable than oxygen produced by OER and the potential risk by H_2/O_2 crossover will also be addressed, eliminating the need for costly separation membrane. From 2016, Ni_2P nanoparticle arrays on nickel foam (Ni_2P NPA/NF) [133], Co-P on copper foam (Co-P/CF) [134], hierarchically porous Ni_3S_2/Ni foam (Ni_3S_2/NF) [135], and hierarchically porous nickel-based electrocatalyst (hp-Ni) [136], were reported in succession as bifunctional electrocatalysts for HMF oxidation coupling with HER by Sun's research group. Recently, Wang and co-workers [143] also put forward a strongly coupled Ni_3N/carbon nanosheets (Ni_3N@C) to proceed with the integration reactions, and evaluated the pathway of

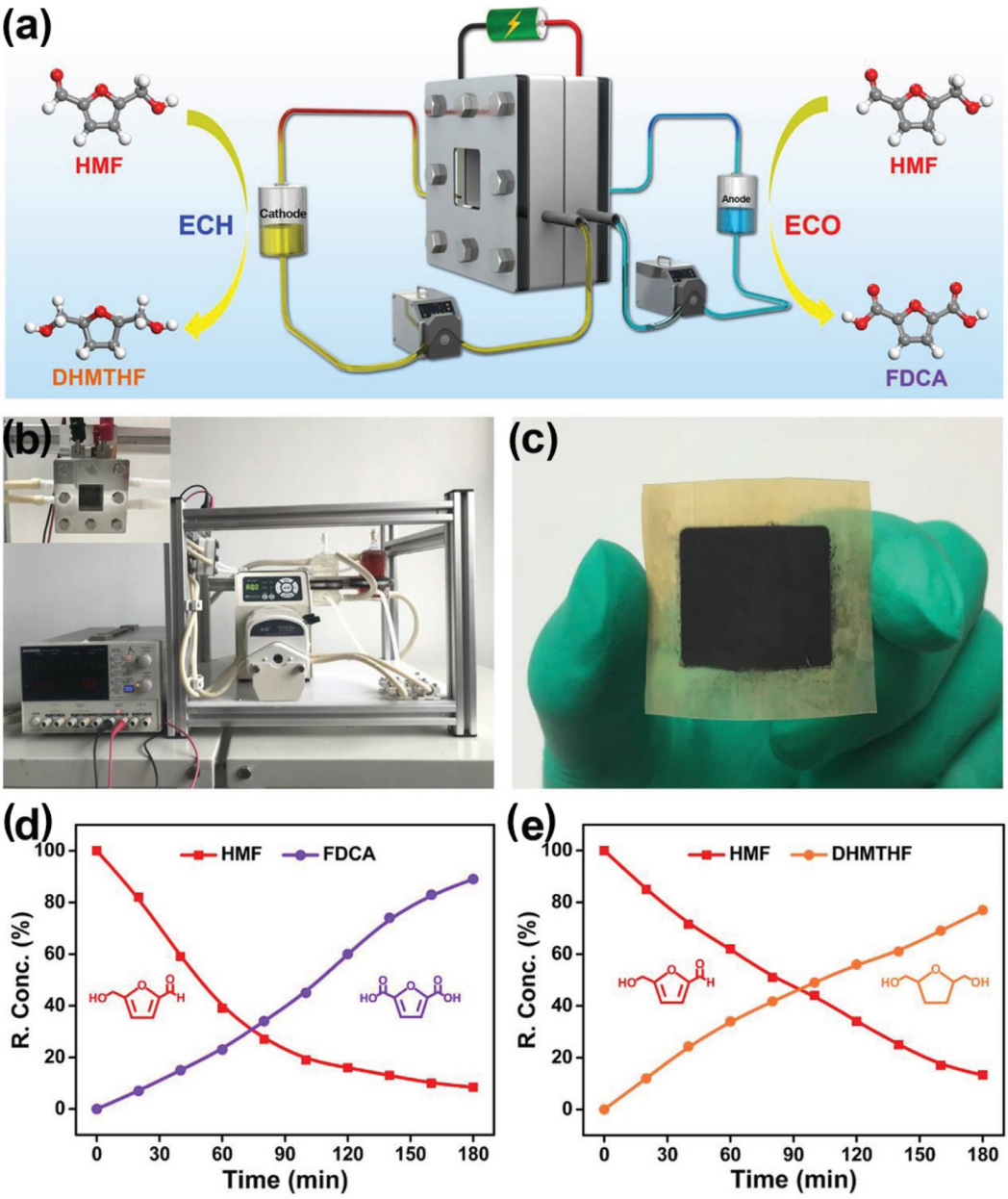


Fig. 11. (a) Scheme of the paired electrolysis of HMF. (b) Photograph of the paired equipment. (c) Catalyst-coated bipolar membrane coated with VN and Pd/VN. (d, e) Concentration variation of HMF, FDCA, and DHMTHF [142]. Copyright 2019, Wiley-VCH Verlag GmbH & Co. KGaA, Weinheim.

HMF oxidation by using sum frequency generation (SFG) vibrational spectroscopy. For all bifunctional electrocatalysts, by passing stoichiometric charge, HMF converted completely to achieve about 98% and 90% yields of FDCA on Ni-based electrodes and Co-P/CF, respectively. The substitution of OER by HMF oxidation enabled the cell voltage significantly reduced by more than 200 mV, demonstrating much better energy conversion efficiency of the integration system relative to water splitting alone. Due to the absence of separation membrane, the possible electro-reduction of reducible –CHO group of HMF is a competitive reaction with HER and thus will appreciably lower the selectivity and faradaic efficiency of cathodic reaction. However, all the four catalysts mentioned above showed nearly 100% FE toward cathodic hydrogen evolution, suggesting there was only water reduction to H_2 on the cathode. This result is relative to the fact that the conversion of HMF are highly dependent on the pH of electrolyte, while electrochemical reduction or hydrogenation of HMF were often reported in acidic [151] or neutural [152] environment. Despite hydrogen generation is more favorable in acidic media than in alkaline media, the combination of HMF oxidation with HER in the acidic electrolyte is rarely reported.

we recently reported Co_3O_4 nanowires as highly efficient bifunctional electrocatalysts for simultaneous oxidation HMF into FDCA and production of hydrogen from water splitting using a similar integration strategy (Fig. 10) [153]. Through a facile hydrothermal reaction and subsequent low-temperature pyrolysis, the well-constructed Co_3O_4 nanowires with pine needle-like shape were in-situ anchored on nickel foam to form 3D monolithic electrode (CoNW/NF). The defective feature of nanowire array with abundant crystals and interconnected pores enabled CoNW/NF with excellent electrocatalytic performance. For OER alone, the linear sweep voltammetry (LSV) curve recorded on CoNW/NF showed 1.563 V vs RHE at the characteristic current density of 10 mA cm^{-2}, superior to most of OER catalysts based on transition metals. After adding HMF to reach 100 mM, the required potential at the benchmark 10 mA cm^{-2} current density was just 1.269 V vs RHE with the corresponding Tafel plots of 125 mV dec^{-1}, demonstrating the highly thermodynamic and kinetic activities of the as-synthesized CoNW/NF catalyst. To our best knowledge, the result is still superior to the vast majority of the reported catalysts for electrooxidation of HMF, such as Ni_2P NPA/NF (1.35 V vs RHE at onset) [133], Ni_3S_2/NF (1.35 V vs RHE at onset) [135], Co-P/CF (1.30 V vs RHE at onset) [134], hp-Ni (~1.35 V vs RHE at onset) [136], Ni_xB/NF (1.38 V vs RHE at onset) [137], Nano-Cu foam (1.25 V vs RHE at onset) [146], $NiCo_2O_4$/NF (~1.36 V vs RHE for 10 mA cm^{-2}) [140], NiFe LDH (1.25 V vs RHE at onset) [127], $CuNi(OH)_2$/C (1.45 V vs RHE for 9.2 mA cm^{-2}) [147], NiSe@NiO_x (1.35 V vs RHE at onset) [148], and MoO_2-FeP@C (1.323 V vs RHE at onset) [154]. For HER, the cathodic LSV curves exhibited no visible difference with and without HMF participation even the concentration of HMF up to 100 mM, contrasted to the situation of NF with 14 mV negative shift when 100 mM presented, indicating CoNW catalyst-equipped with a high preference for hydrogen formation rather than the possible reduction of aldehyde groups of HMF and intermediates. Further product analysis revealed that, 100% HMF conversion and H_2 evolution FE, as well as 96.8% yield and 96.6% FE toward FDCA production, were achieved on the 3D CoNW/NF catalyst in individual three-electrode reactions. More importantly, the pine needle–like features displayed excellent structural stability and robust catalytic durability for five successive electrolysis cycles for ~ 30 h in total. For the integration of HMF oxidation and HER, the two-electrode system containing 1.0 M KOH and 100 mM HMF required a cell voltage of only 1.504 V to achieve a current density of 10 mA cm^{-2}, reducing by 362 mV in comparison

Table 6
Representative electrocatalytic performance of HMF oxidation into FDCA in aqueous electrolyte.

Electrodes	HMF	Time	Charge	Electrolyte	Potential (V vs. RHE)		Conversion[a]	Yield	FE[b]	Ref.
	(mM)	(h)	(C)		Onset	Constant potential electrolysis	(%)	(%)	(%)	
Pd_1Au_2/C	20	1	NA[c]	0.1 M KOH	0.30	0.9	100	83	-	[63]
NiOOH	5	4	NA[c]	1 M NaOH	-	0.6 V vs SCE	-	71	84	[132]
$NiCo_2O_4$/NF	10	2.7	35	0.1 M KOH	1.35	1.55	~100	~90	99	[140]
$NiCo_2O_4$/NF	5	~40 min	34.75	1 M KOH	~1.2	1.5	99.6	90.4	87.5	[141]
NiOOH/FTO	5	4.7	40.52	0.1 M KOH	-	1.47	99.8	96	96	[144]
CoOOH/FTO	5	22	40.52	0.1 M KOH	-	1.56	95.5	35.1	35.1	
FeOOH/FTO	5	2.3	40.52	0.1 M KOH	-	1.71	16	1.59	1.59	
MnO_x	20	NA[c]	250	0.05 M H_2SO_4	-	1.6	99.9	53.8	33.8	[150]
Ni_2P NPA/NF	10	NA[c]	~59	1 M KOH	1.35	1.423	100	98	98	[133]
Co-P/CF	50	6	~560	1 M KOH	1.3	1.423	100	~90	-	[134]
Ni_3S_2/NF	10	NA[c]	~58	1 M KOH	1.35	1.423	100	98	98	[135]
hp-Ni	10	NA[c]	~58	1 M KOH	~1.35	1.423	100	98	98	[136]
Ni_3N@C	10	NA[c]	180	1 M KOH	1.35	1.45	100	98	99	[143]
CoNW/NF	100	5.73	289.5	1 M KOH	-	1.72[d]	100	96.8	96.6	[153]
Ni_xB/NF	10	30 min	58.2	1 M KOH	1.38	1.45	100	98.5	100	[137]
NiB_x/NF	10	100 min	NA	1 M KOH	-	0.6 V vs SHE	99.8	99.8	99.5	[139]
NCF	5	NA[c]	41	0.1 M KOH	1.25	1.62	99.9	96.4	95.3	[146]
NiFe LDH	10	1.5	NA[c]	1 M KOH	1.25	1.33	98	98	98.6	[127]
Ni/NiOOH	650	18	120 k	0.1 M Na_2SO_4	-	1.55	100	89	80	[145]
VN/NF	10	55 min	NA[c]	1 M KOH	1.36	20 mA[e]	98	96	84	[142]
$CuNi(OH)_2$/C	5	NA[c]	90	1 M KOH	1.38	1.45	98.8	93.3	94.4	[147]
CoB/NF	10	1	58.8	1 M KOH	1.39	1.45	100	94	98	[138]
NiSe@NiO_x	10	NA[c]	~58	1 M KOH	1.35	1.423	100	99	99	[148]
Cu_xS@NiCo-LDH	10	~1.25	~58	1 M KOH	1.19	1.32	100	99	99	[149]
MoO_2-FeP@C	10	~2.7	116	1 M KOH	1.323	1.424	99.4	98.6	97.8	[154]
BNC	5	6	NA[c]	0.1 M NaOH	-	1.9	71	57	-	[160]

[a] conversion of HMF
[b] faradaic efficiency for FDCA
[c] not available
[d] cell voltage.
[e] cell current.

with that of water oxidation. On account of such catalytic activities, the energy-saving coupling configuration was also visually demonstrated by using a commercial 1.5 V battery as a driven force, unambiguously verifying the concept of energy barrier reduction by substitution OER with HMF oxidation.

Except for the substitution of OER by HMF oxidation on the anode, the cathodic HER in the coupling system can also be replaced by hydrogenation [155–158] of HMF or other organic molecules, arising a new route to the paired electrosynthesis by using water as an oxygen and hydrogen source. For instance, Wang and co–workers [142] recently succeeded in simultaneous electrocatalytic oxidation (ECO) and electrocatalytic hydrogenation (ECH) of HMF into FDCA and 2,5-bishydroxymethyl-tetrahydrofuran (DHMTHF), respectively, by using a membrane electrode assembly electrolyzer. As depicted in Fig. 11, the core of the paired electrosynthesis system was actually a membrane reactor consisting of two separate compartments and a bipolar membrane, achieving entirely different electrochemical environments due to the excellent tolerance of the membrane to different pH values. Vanadium nitride (VN) and Pd/VN were sprayed on both sides of the bipolar membrane to act as ECO catalyst and ECH catalyst, respectively. By employing two pumps to separately circulate the anolyte and catholyte, the paired electrolyzer realized 92% and 87% conversions, as well as ~ 89% and ~ 77% yields, for HMF oxidation and hydrogenation, respectively. Although two catalysts were incorporated into a bipolar membrane to form an electrode assembly, rather than one component acted as a bifunctional catalyst, the 3D hollow nanosphere structure of VN played a critical role in

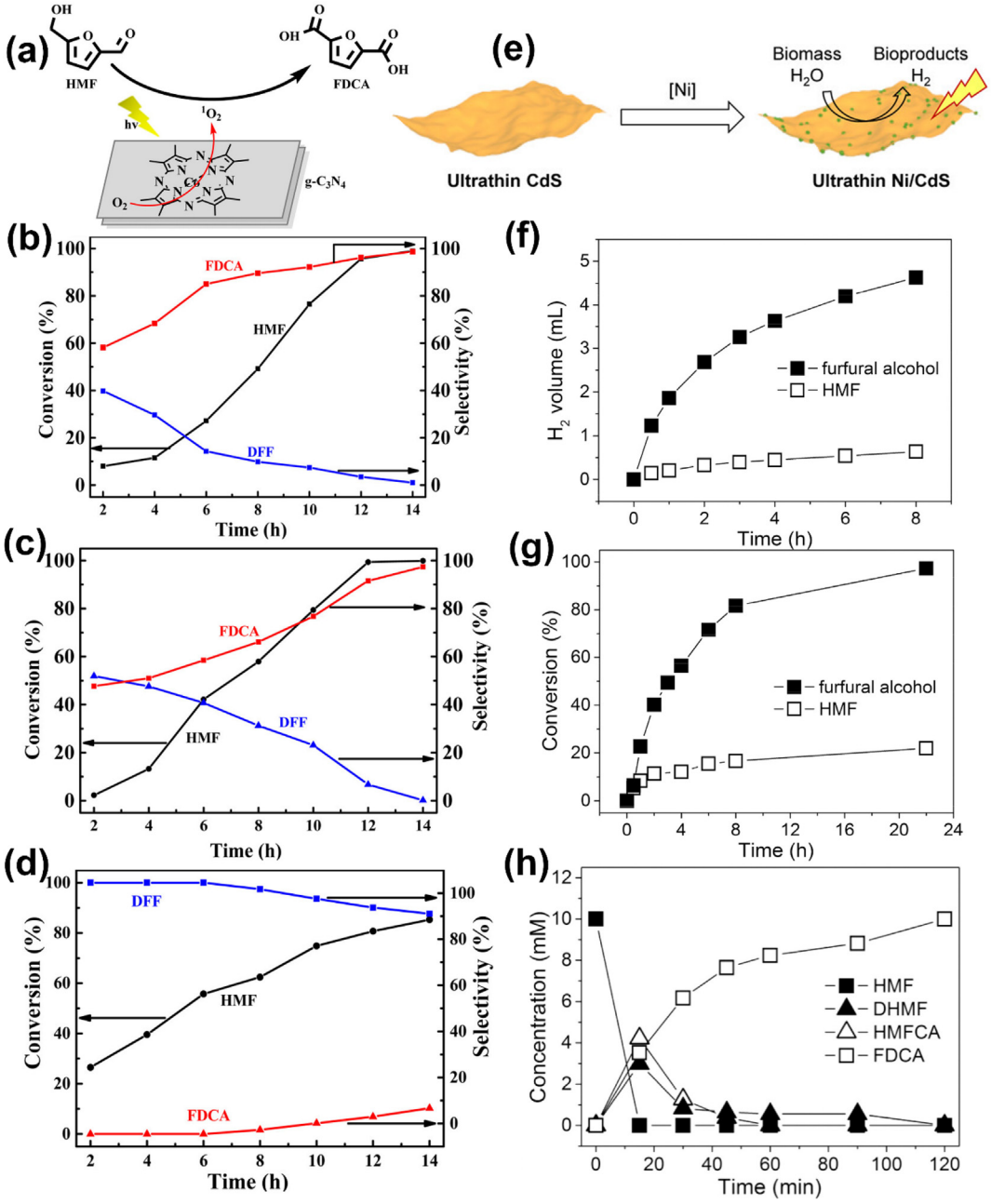


Fig. 12. (a) Scheme for the photocatalytic oxidation of HMF into FDCA and (b-d) the influence of reaction system pH on the photocatalytic performance over CoPz/g-C_3N_4 [81]. (e) Synthesis of Ni/CdS photocatalyst for integrated (f) H_2 production and biomass conversion in (g) neutral water and (h) alkaline solution [164]. Copyright 2017, American Chemical Society.

the diffusion and transportation of the substrate in both ECO and ECH reactions. On the other hand, for the situation of furfural without –CH_2OH attached to the furan ring, Zhao et al. [159] recently found the carbon fiber cloth supported Cu_3P nanosheets and granular Ni_2P nanocrystals (Cu_3P/CFC and Ni_2P/CFC, respectively) were of electrocatalytic activities for both furfural hydrogenation reaction (FHR) and furfural oxidation reaction (FOR) in alkaline media. Due to the fact that Ni_2P/CFC is more favorable for FOR and Cu_3P/CFC is more favorable for FHR, a two-electrode H-type electrocatalysis cell assembled with Ni_2P/CFC as anode and Cu_3P/CFC as cathode was constructed for simultaneous electrosynthesis of furfuryl alcohol and furoic acid with ~ 100% selectivity in 1 M KOH solution, demonstrating high FE of 97%–99%. By applying NiB_x as a bifunctional catalyst in 1 M KOH electrolyte, Sun et al. [139] also progressed in paired electrolysis for the simultaneous oxidation of HMF to FDCA and hydrogenation of *p*-nitrophenol to *p*-aminophenol, acquiring ≥ 99% conversion efficiency and selectivity. Qin et al. [160] recently reported a novel B and N codoped porous carbon (BNC) as the first metal-free electrocatalyst for HMF oxidation coupling with N_2 reduction reaction (NRR). After 6 h electrolysis at a relatively high anode potential of 1.9 V vs RHE, FDCA was successfully obtained with a yield of 57% at 71% conversion of HMF. However, among these paired electrolysis systems, the shuttles or crossover of organic substrates and intermediates even products often cause serious side reactions thus lower the FE of objective reactions, arousing the use of separate membrane again. Table 6 enumerates the representative electrochemical oxidations of HMF. The conversion and yield, as well as FE toward FDCA production, given in the table are the best achieved under the desired conditions.

4. Photoelectrocatalytic and photocatalytic oxidation of HMF

4.1. Photoelectrocatalytic oxidation

Considering the inexhaustible solar energy, it is undoubtedly more attractive to accomplish HMF oxidation and H_2 production by directly introducing external light as the energy source to the above electrolysis, instead of electrolysis powered by photovoltaic electricity. In 2015, Choi et al. [161] constructed a photoelectrochemical cell (PEC) with 2,2,6,6-tetramethylpiperidine 1-oxyl (TEMPO) as a mediator and catalyst to utilize solar energy for HMF photooxidation and H_2 generation. In the fabricated PEC, the nanoporous n-type $BiVO_4$ photoanode generated and separated hole-electron pairs under simulated solar illumination. The photogenerated holes oxidized TEMPO to $TEMPO^+$, which was highly active to oxidize HMF to form final FDCA in alkaline media, whereas the photoexcited electrons were transferred to the Pt counter electrode by external bias to reduce water to H_2. The high FE and yield for FDCA formation, up to 93% and 99%, respectively, indicated that TEMPO-mediated HMF oxidation was kinetically much faster than OER and was the dominant oxidation reaction, even in the pure electrocatalytic reaction [162]. The vital role of $BiVO_4$ is providing a suitable valence-band (VB) to generate holes to initiate TEMPO oxidation, demonstrated by the photocurrent onset potential was shifted to 0.32 V vs RHE while the electrochemical onset potential was 1.01 V vs RHE. Motivated by substituting the kinetically unfavorable OER and producing value-added FDCA in PECs, Li and co-workers [163] recently reported a cobalt phosphate (CoPi) modified $BiVO_4$ to further improve the performance of TEMPO-mediated HMF oxidation. The authors confirmed the heterostructured $BiVO_4$/CoPi photoanodes and the electrodeposition time was a critical parameter for controlling the thickness of CoPi and thus selectively promoting TEMPO oxidation. $BiVO_4$/CoPi prepared by a 30 min CoPi deposition ($BiVO_4$/CoPi-30) was found to reduce the potential required for TEMPO oxidation by about 0.5 V, as well as improve the charge injection efficiency sevenfold compared to bare $BiVO_4$. Furthermore, O_2 was not detected for $BiVO_4$/CoPi-30, suggesting the greater selectivity towards TEMPO oxidation without any faradaic efficiency loss to OER. Transient photocurrent measurements demonstrated that CoPi inhibited solution-mediated recombination resulting from the back reduction of oxidized TEMPO, which was identified as the bottleneck factor for $BiVO_4$ performance. Although the above two works opened up a bright future for exploration of rationally-designed photoanodes and new reaction routes to more fully and efficiently utilize renewable solar energy and renewable feedstocks, the drawback of TEMPO-mediated method cannot be ignored. Compared to pure electrochemical oxidation, the additional requirement of a greater proportion of TEMPO (≥1 equivalent) for higher FDCA yield makes the TEMPO-mediated process highly expensive. Moreover, due to the good solubility of TEMPO, the separation and purification of final FDCA from homogeneous TEMPO are difficult. Immobilization of TEMPO on heterogeneous supports will reduce these barriers. In addition, the reported high yield and FE toward FDCA yield are based on a low initial concentration of HMF, so the photoelectrochemical field is critical to developing more robust catalysts to efficiently convert HMF to FDCA.

4.2. Photocatalytic oxidation

On account of the overpotential for photoanode oxidation is determined by the VB edge position of semiconductor and the role of the applied bias for PEC is only to enhance the separation of photogenerated hole-electron to make more holes available for oxidation, it is possible to develop better photocatalysts to achieve pure photocatalysis without external bias and TEMPO. In 2017, Zhang et al. [81] exploited a hybrid photocatalyst for the selective oxidation of HMF into FDCA by immobilizing cobalt thioporphyrazine (CoPz) on g-C_3N_4 (CoPz/g-C_3N_4) (Fig. 12a). The biomimetic CoPz itself has some unique capacity in photocatalytic activation of triplet oxygen ($^3O_2$) to generate singlet oxygen ($^1O_2$), which has appropriate oxidizing power to convert HMF into the desirable FDCA. Nevertheless, CoPz molecules are prone to aggregate in aqueous solution due to their hydrophobicity, reducing the contact between the catalyst and HMF reactant and thus giving a very modest catalytic performance with 40.2% conversion and 36.2% yield after 14 h UV–visible irradiation (300–1000 nm Xe light, 0.5 W/cm^2). On the other hand, semiconductive g-C_3N_4 is often used as an active photocatalyst for water splitting and pollution degradation. However, no furan product could be detected at HMF conversion of 99.6% when g-C_3N_4 used as photocatalyst alone, which means that the pure g-C_3N_4 is not suitable for the selective oxidation due to the degradation of HMF to CO_2 and H_2O by the g-C_3N_4 generated hydroxyl radicals (HO•). After dispersed CoPz on g-C_3N_4, the strong interaction between the two components not only improves accessibility and $^1O_2$ generation ability of the CoPz sites but also suppresses the HO• generation by g-C_3N_4, significantly enhancing the photocatalytic performance to obtain 96.1% FDCA yield under the same irradiation conditions using air as a benign oxidant. In addition, the pH value of the reaction system has been found to play a critical influence on the selectivity of the final oxidation products (Fig. 12b-d). At pH = 9.18 or 6.86, the main product after 14 h reaction was FDCA with high selectivity more than 95%, while at pH = 4.01 HMF selective produced DFF with a yield of above 80%. Combined that the selectivities of DFF at the initial 2 h were more than 45% in the three reaction systems with different pH values, the photocatalysis on CoPz/g-C_3N_4 was inferred to undergo DFF-intermediated route and possible to select the final product by adjusting the reaction system pH. Analogous regulation of product by control of pH was also reported later by Sun et al.

Table 7
Photoelectrocatalytic and photocatalytic performance of HMF oxidation into FDCA.

Photoelectrodes/ Photocatalysts	Light source	HMF	T[a]	Reaction conditions[b]	Conversion[c]	Yield	Reaction rate		Ref.
		(mM)	(°C)		(%)	(%)	(mmol g_{cat}^{-1} h^{-1})		
							HMF	FDCA	
$BiVO_4$ electrode	AM 1.5G illumination (100 mW cm^{-2})	5	NA[d]	7.5 mM TEMPO in 0.5 M borate buffer solution (pH = 9.2), 1.04 Vvs. RHE at 40C	99.24	98.85	-	-	[161]
$BiVO_4$/CoPi-30 electrode	AM 1.5G illumination (100 mW cm^{-2})	1	NA	5 mM TEMPO in sodium borate electrolytes (pH = 9.2), 0.64 V vs. RHE, 2.7 h	98.8	88	-	-	[163]
CoPz/g-C_3N_4	300–1000 nm Xe light (0.5 W cm^{-2})	20	RT[e]	$Na_2B_4O_7$ buffer solution (pH = 9.18), 0.1 MPa air, 14 h	99.1	96.1	11.326	10.983	[81]
Ni/CdS	440–460 nm blue LED (8 W)	10	NA	10 M NaOH, 2 h	~100	~100	~5	~5	[164]
ZnO/PPy	450 nm LED (102 W cm^{-2})	8	25 40	aqueous media (pH = 7.8)0.1 MPa air, 6 h	~5 30	1.52 ~5.4	~0.2 1.2	0.061 0.216	[165]

[a] reaction temperature.
[b] reaction conditions including electrolyte, applied bias, solvent, pressure, reaction time.
[c] conversion of HMF.
[d] not available.
[e] room temperature.

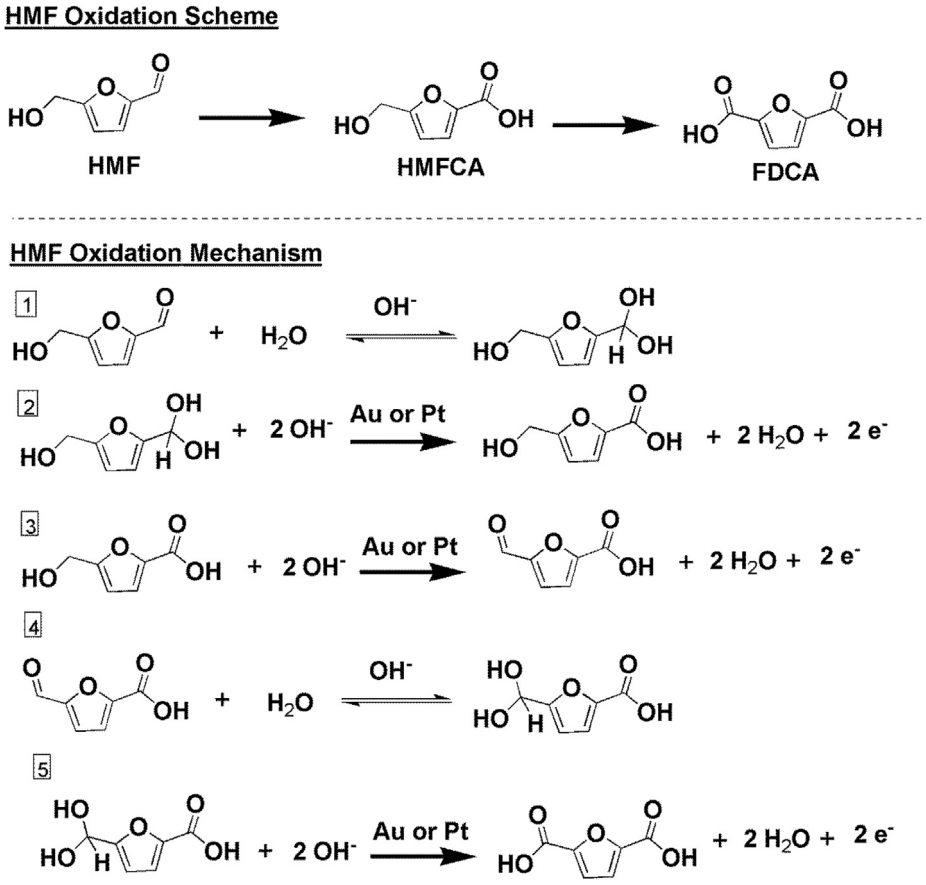


Fig. 13. Reaction mechanism for the oxidation of HMF in alkaline solution [166]. Copyright 2012, The Royal Society of Chemistry.

[164], who ascribed the results to the Cannizzaro mechanism that –CHO groups will disproportionate to form corresponding –OH and –COOH in alkaline environment. Using Ni decorated ultrathin 2D CdS nanosheets (Ni/CdS) as a photocatalyst, the authors developed a photocatalytic integration strategy to efficiently utilize the photoexcited holes and electrons to oxidize biomass substrates and simultaneously reduce protons to H_2, respectively (Fig. 12e). Under the visible light irradiation (440–460 nm blue LED, 8 W) for 2 h, HMF was utterly transformed to FDCA with concomitant generation of H_2 in the presence of 1000 equiv. NaOH, while furfural alcohol exhibited a faster oxidation to yield over 90% furoic acid in only 1 h under the same conditions (Fig. 12f-h). Further control experiments with 2,5-dihydroxymethylfurfural (DHMF) and HMFCA as reaction substrates verified that, the presence of an –CHO group seemed to impede the oxidation of –OH attached to the furan ring, whereas ancillary –OH and –COOH groups did not present any negative impact. More importantly, according to the results of photoluminescence and ^{1}H NMR detection, almost no HO• radicals were generated during the photocatalysis process, which is highly consistent with the situation of CoPz/g-C_3N_4. In addition, the negative

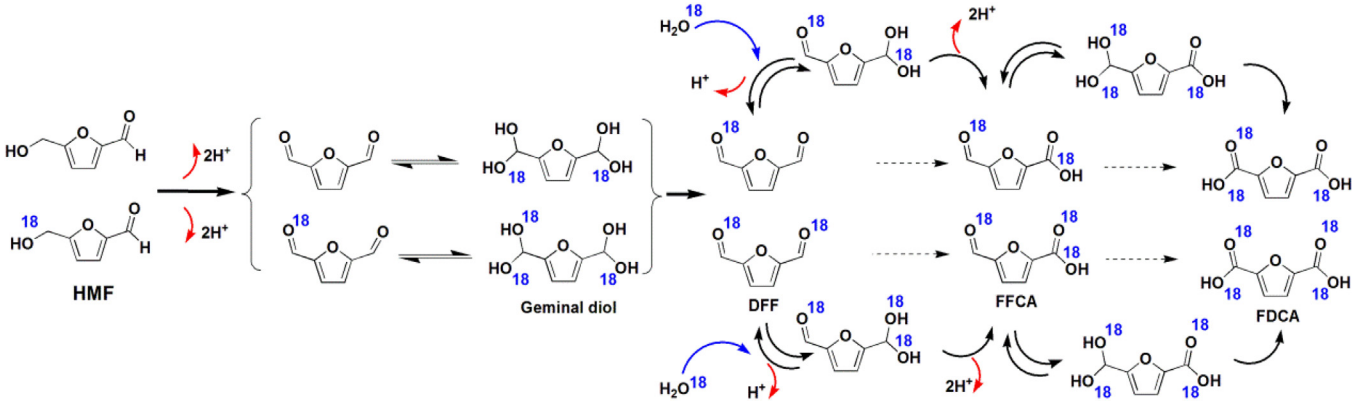


Fig. 14. Incorporation of ^{18}O in the base-free oxidation of HMF [167]. Copyright 2014, Elsevier.

Table 8
Reaction mechanism and catalytic cycles for HMF oxidation [53]. Copyright 2019, American Chemical Society.

Step	Reaction	Const symbol
A	$O_2 + 2\sigma \rightleftharpoons 2O\sigma$	K_{O2}
B	$OH + \sigma \rightleftharpoons OH\sigma$	K_{OH}
C	$HMF + \sigma \rightleftharpoons HMF\sigma$	K_{HMF}
D	$HMF\sigma + OH\sigma \rightleftharpoons Int.1\sigma + \sigma$	$K_{Int.1}$
E	$Int.1\sigma + \sigma \rightarrow HMFCA\sigma + H\sigma$	k_1
F	$HMFCA\sigma + OH\sigma \rightleftharpoons Int.2\sigma + H_2O\sigma$	$K_{Int.2}$
G	$Int.2\sigma + OH\sigma \rightarrow FFCA\sigma + H_2O\sigma$	k_2
H	$FFCA\sigma + OH\sigma \rightleftharpoons Int.3\sigma + \sigma$	$K_{Int.3}$
I	$Int.3\sigma + \sigma \rightarrow FDCA\sigma + H\sigma$	k_3
J	$H\sigma + O\sigma \rightleftharpoons OH\sigma + \sigma$	K_H
K	$HFMCA\sigma \rightleftharpoons HMFCA + \sigma$	K_{HMFC}
L	$FFCA\sigma \rightleftharpoons FFCA + \sigma$	K_{FFCA}
M	$FDCA\sigma \rightleftharpoons FDCA + \sigma$	K_{FDCA}
N	$H_2O\sigma \rightleftharpoons H_2O + \sigma$	K_{Wat}

impact of HO• radicals can also be revealed by the partial oxidation of HMF on a composite photocatalyst of ZnO and polypyrrole (ZnO/PPy) in pH = 7.8 water solution [165]. The presence of HO• radicals on the surface of the ZnO/PPy photocatalyst was proved by the determination with terephthalic acid. Under the visible light irradiation by a 15 W LED for 6 h, the conversion of HMF was 5% and 30% at 25 and 40 °C, while the selectivity of FDCA was reduced from 30 to 18%, respectively. The decreased selectivity to HMFCA, DFF, and FDCA indicates that the increase of photocatalysis temperature is unfavorable for any desirable furan products, which is mainly due to the non-selective oxidation by the highly reactive radicals became more intense at the higher temperature to crack the furan ring even mineralize HMF. The photoelectrocatalytic and photocatalytic performance of HMF oxidation into FDCA are enumerated in Table 7.

5. Mechanism of catalytic oxidation of HMF

As shown in Scheme 1, the liquid phase oxidation of HMF over supported metal catalysts is a parallel-consecutive process, which is mainly due to the hydroxyl group and aldehyde group on furan ring equipped with close initial oxidation potential (the former is 0.55 V and the latter is 0.58 V vs. RHE on the Pd/C electrode) [63]. Additionally, the surface chemistry of catalysts can obviously affect the adsorption of HMF on the catalyst, thus affecting the subsequent catalytic reactions. A large number of researchers monitored the concentration variation of HMF, detectable intermediates (DFF, HMFCA, and FFCA) and final product FDCA, to deduce the catalytic oxidation routes. However, most of them failed to put forward a definite and convincing reaction mechanism so far.

Recent advances in the oxidation mechanism of HMF have made significant and substantial progress by means of isotope labeling technology. In 2012, Davis et al. [166] studied the mechanism of HMF oxidation into FDCA over supported Au and Pt catalysts using isotope labeling. The aerobic oxidation of HMF catalyzed by Au/TiO_2 at 22 °C and 345 kPa O_2 with 2 equivalents of NaOH gave more than 98% selectivity of HMFCA after 6 h. To figure out the role of O_2, the oxidation of HMF was performed using $^{18}O_2$ as an oxidant, but there was no detectable ^{18}O in the product HMFCA. As a comparison, the oxidation of HMF was undertaken in the $H_2^{18}O$ solvent. As expected, 1 ^{18}O atom was incorporated into HMFCA. The results revealed that water was the source of oxygen atoms in HMF oxidation through the catalytic conversion of hydroxide. First, a geminal diol was formed via the nucleophilic addition of a hydroxide ion from water to the carbonyl (Fig. 13, step 1). Then OH^- promoted O–H and C–H bond activation of the alcohol side chain of HMF in the presence of Au or Pt metal catalysts (Fig. 13, steps 2, 3) and at last oxidized aldehyde intermediates analogously to step 1 and 2 to form final diacid products (Fig. 13, steps 4, 5).

The above pathway of HMF oxidation was often proposed in the similar aqueous alkaline system catalyzed by Au, Pt, Pd, and their alloys, mainly based on the intermediate products that were detected to be HMFCA and FFCA. However, the reaction pathway of aerobic oxidation of HMF was somewhat different when the reaction conditions changed, such as catalysis by Ru catalysts [33,115,123], absence of base additives, use of organic solvents. In 2014, Siankevich et al. [167] studied the oxidation mechanism of HMF catalyzed by Pt nanoparticles in water using ^{18}O isotope labeling technology with the kinetic method. It was found that DFF and FFCA appeared in the oxidation reaction and HMFCA was not observed in the base-free system. As illustrated in Fig. 14, ^{18}O atoms supplemented in the intermediates DFF, FFCA and final product FDCA were derived from the labeled $H_2^{18}O$. Molecular O_2 was essential for HMF oxidation by scavenging electrons and the degraded pathway components from catalyst surface and thus enhancing the rates of each catalytic step.

Besides reaction pathways, unraveling elementary steps and kinetic parameters is another key to understanding catalytic reaction mechanisms. Recently, Ferreira et al. [53] conducted a kinetics investigation for HMF oxidation to FDCA based on a Langmuir-Hinshelwood-Hougen-Watson (LHHW) mechanism and pseudo-equilibrium approach. A continuous process in a trickle-bed reactor was used to investigate the aqueous phase oxidation over Ru/Al_2O_3 in aqueous Na_2CO_3 feed. The sequence of elementary steps

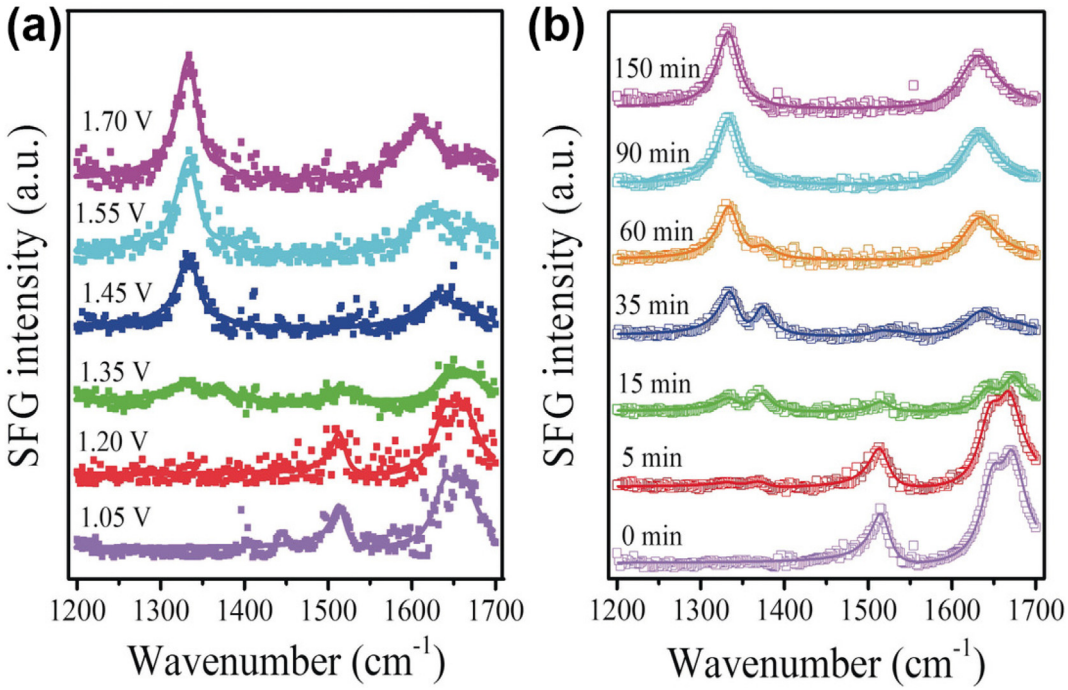


Fig. 15. In-situ SFG spectra recorded (a) at various voltages for 90 min electrolysis and (b) at different times at a constant 1.45 V vs. RHE in 1 M KOH with 20 mM HMF [143]. Copyright 2019, Wiley-VCH Verlag GmbH & Co. KGaA, Weinheim.

for the HMF oxidation was proposed in Table 8 considering metallic Ru^0 species as the single active site (σ). Considering the similar reaction pathway (HMF → HMFCA → FFCA → FDCA), the apparent activation energies for the oxidation of HMF, HMFCA, and FFCA, were estimated to be 32.1 kJ/mol, −25.1 kJ/mol, 58.7 kJ/mol, respectively. The model provided much higher values for k_2 than for k_1, due to HMFCA was consumed quickly. At the optimized temperature of 140 °C, k_3 got to a higher value than k_1, indicating that high temperatures were needed to over the energy barrier for the final oxidation. The obtained activation energies and rate constants confirmed that the oxidation of FFCA to FDCA was the rate-limiting step in the reaction, which agreed with the observed product distribution. The type and concentration of base played a significant role in the initial dehydrogenation step, whereas high oxygen pressure favored to achieve a high selectivity toward FDCA. However, Liu et al. [33] reported a different kinetic study on Ru/C involving DFF intermediate, rather than HMFCA. The rate constants revealed the FFCA oxidation to FDCA was much smaller (2.49×10^{-6} s^{-1}) than those of HMF oxidation to DFF and DFF to FFCA (9.15×10^{-5} s^{-1}, 8.05×10^{-5} s^{-1}, respectively). Accordingly, the activation energies of the three oxidation steps were 52.5, 34.2, and 38.6 kJ/mol, respectively. Although HMFCA was not detected as intermediate, the oxidation of FFCA to FDCA was still the rate-determining step to dictate the formation rate of FDCA from HMF. The results were consistent somewhat with the previous study by Besson et al., using a power-law model to fit experimental data on Pt/TiO_2 catalyst [37]. Under base-free conditions, the oxidation occurred mainly by the oxidative dehydrogenation of $–CH_2OH$ of HMF to form –CHO as the major products were DFF and FFCA. Increasing amounts of the base not only neutralized –COOH but also accelerated the oxidation rates of –CHO in the intermediates to the final FDCA. The higher rate constant for HMF oxidation to DFF than to HMFCA suggested the predominant formation of the DFF intermediate in this system. However, –CHO reacts very rapidly in basic solution to yield FFCA and thus the concentration of DFF is often very low, consisting with the high turnover frequency of 48 h^{-1} for DFF compared with 4 h^{-1} for HMF [36]. Using MFe_2O_4 (M = Cu, Mn, Co, Mg) as catalysts along with t-BuOOH as a stoichiometric oxidant without external base additive, Yadav et al. [44] analyzed the kinetics of HMF oxidation and pointed out that the oxidation of $–CH_2OH$ to –CHO is faster than oxidation of –CHO to –COOH. Above all, the reaction pathway and rates are very sensitive to the catalyst nature and reaction environment.

Taking into consideration of the fact that the pathway of HMF oxidation was usually interpreted based on ex-situ detection and the essence of a redox reaction is electron transfer, it is reasonable to investigate the relationship of the conversion intermediates with the potential of the HMF electrooxidation by in situ technique. Very recently, Wang et al. [143] studied the conversion path of HMF on Ni_3N@C electrocatalyst in 1.0 M KOH, via an in-situ sum frequency generation (SFG) vibrational spectroscopy to observe the change of organic species in during the electrocatalytic oxidation (Fig. 15). The in situ SFG approach is a second-order nonlinear optical technique with interface selectivity and sensitivity, and very suitable for identifying the molecular structure at the interface without influence from the electrode. After running the electrolysis at different potentials for 90 min, the SFG spectrum revealed that HMF was stable at the potential below 1.25 V, and began to oxidize to HMFCA when the potential reached to 1.35 V. As the potential increased to 1.45 V, the dominated 1335 cm^{-1} peak accompanied by the red-shift of the C=O stretching band was assigned to the formation of FFCA or FDCA. At 1.75 V, the product appeared almost characteristic peaks identical to pure FDCA with C=O stretching peak at around 1610 cm^{-1}, suggesting the conversion of HMF was completed to the final FDCA rather than stayed at the intermediate FFCA step. For the constant potential electrolysis at 1.45 V, the characteristic peaks of HMFCA appeared at 15 min and strengthened to the most significant at 35 min. As the electrolysis time continued to increase, the peak of the intermediate product gradually disappeared, and the peak intensity of FDCA increased

to reach a constant level after 90 min. The in situ SFG results were well consistent with the HPLC analysis, verifying that the HMF electrolysis underwent the HMFCA pathway.

Although some important information about the production of FDCA from HMF oxidation in the base or base-free system is acquired by isotope labeling technique, elementary steps modeling, and in situ SFG approach. It is necessary to use other advanced technologies, such as in-situ electron microscopy and surface chemistry, to further investigate the details of the reaction interfaces and the intrinsic kinetics, as well as the structure–activity relationship. In addition, the oxidation path and kinetics in acidic media have rarely been studied. A comprehensive understanding of the reaction mechanism helps to rationally design more efficient and stable catalysts for HMF oxidation.

6. Conclusions and outlook

Catalytic synthesis of high value-added chemicals from biomass-derived platform chemicals is not only objectively necessary but also actually possible to reduce current dependence on fossil-fuel resources. Efficient oxidation of HMF into FDCA in a heterogeneous manner mainly proceeds through thermocatalytic, electrocatalytic, and photocatalytic techniques. These catalysis strategies have their own advantages and disadvantages. Thermocatalysis is more commonly used compared to other strategies due to its efficient and convenient procedures. Besides, there are more candidate catalysts to choose for thermocatalysis in alkaline and neutral even acidic mediates, including highly active metals and metal-free carbon catalysts. However, the degradation of the substrate HMF will exacerbate as thermocatalysis often operated at the elevated reaction temperature. Electrocatalytic oxidation is a cleaner and safer method for FDCA production because it eliminates the use of high-pressure oxidizing atmosphere or other environmentally unfriendly chemical oxidants. Driven by the external potential, electrocatalysis shows significant advantages to utilize cheap transition metals as highly active catalysts and solve the thermodynamic and/or kinetic issues in thermocatalysis and photocatalysis. By controlling the electrode potential and circuit current, the management of electrocatalytic reaction parameters can be realized more accurately and conveniently compared to thermocatalysis. Despite many distinct advantages, what we should not ignore is that the conductive electrolyte is often a necessity for electrocatalysis due to the poor conductivity of HMF aqueous solution, causing energy consumption for product separation in the downstream processes compared to base-free heterogeneous catalysis. Photocatalytic and photoelectrocatalytic oxidations have a natural advantage in energy injection because of the use of photon rather than thermal and electrical energy. However, it is very challenging to design and screen efficient photocatalyst with suitable structures for conversion HMF into the desired product. The photogenerated holes and the derivative radicals have a high potential to oxidize organics till completely mineralize to CO_2 [168], whereas photocatalytic HMF-to-FDCA conversion just requires moderately active species such as singlet oxygen to achieve the selective oxidation. Therefore, the core of photocatalysis is to improve the selectivity toward the target products. Overall, the laboratory-scale investigation of HMF oxidation has been relatively abundant, with transferring from traditional homogeneous base systems to heterogeneous base even to base-free systems, gradually realizing the goal of green and sustainable chemistry. But so far, the industrially large-scale and economical oxidation of HMF into FDCA still needs to be improved. More effort should be devoted to the development of highly efficient and economical catalysts, optimization of the reaction process, as well as isolation and purification of products.

First, the activity of non-noble metal catalysts and the stability of noble metal catalysts need to be improved, which are very important for the practical prospects of FDCA production. Second, solvent and base play a crucial role in the reaction pathway and product distribution of HMF oxidation. Although the main oxidative product in the aqueous phase is often FDCA, the decrease in the selectivity of the target product caused by side reactions or competing reactions should not be neglected. Basic additives provide high yields and selectivities to FDCA with fast rates but more complex downstream separations, whereas reactions in neutral systems often suffer serious hold-up and product inhibition due to insoluble FDCA covering on the catalyst [124]. Third, the batch stirring tank reactor was applied in most reports [43,169–171], but there are some shortcomings, such as inconvenient operation, low productivity, and lower economy. For the sake of continuous and large-scale production in the future, gas–liquid-solid three phases fixed-bed reaction process is an alternative technology worth studying to overcome the above disadvantages of batch reaction. Fourth, the development of electrochemical oxidation is expected to change the overall situation of traditional thermal catalysis, but how to exclude the use of high-concentration base or acid electrolytes is still a long way to go. Fifth, the activity of metal-free catalysts needs to be greatly improved, and it is also an important aspect to develop high-efficiency activity regulation methods, such as introducing light and microwave into the reaction system. Sixth, from the economic perspective, HMF as a substrate is still too expensive to produce furan derivates. Biomass carbohydrates, such as glucose, fructose, and cellulose, are of great significance in the synthesis of FDCA, which has also received great attention and is facing many challenges in a complex operation and low yields. Last but not least, a comprehensive understanding of the reaction mechanisms of HMF oxidation is one of the most important research cores in the biomass conversion field, which helps to create original innovations in catalyst design and reaction engineering.

Declaration of Competing Interest

The authors declare that they have no known competing financial interests or personal relationships that could have appeared to influence the work reported in this paper.

Acknowledgments

This work was supported by Chinese Academy of Sciences (QYZDB-SSW-JSC037), Natural Science Foundation of Zhejiang Province (LY19B030003, LQ19B060002), Ningbo Science and Technology Bureau (2018B10056, 2019B10096), and Fujian Institute of Innovation (FJCXY18020202).

References

[1] A.J. Ragauskas, G.T. Beckham, M.J. Biddy, R. Chandra, F. Chen, M.F. Davis, B.H. Davison, R.A. Dixon, P. Gilna, M. Keller, P. Langan, A.K. Naskar, J.N. Saddler, T.J. Tschaplinski, G.A. Tuskan, C.E. Wyman, Science 344 (2014) 1246843.
[2] A. Corma, S. Iborra, A. Velty, Chem. Rev. 107 (2007) 2411–2502.
[3] M.A. Ayude, L.I. Dournic, M.C. Cassanello, K.D.P. Nigam, Ind. Eng. Chem. Res. 58 (2019) 16077–16095.
[4] M. Sajid, X.B. Zhao, D.H. Liu, Green Chem. 20 (2018) 5427–5453.
[5] Y. Yang, Q.Y. Liu, D. Li, J. Tan, Q. Zhang, C.G. Wang, L.L. Ma, RSC Adv. 7 (2017) 16311–16318.
[6] B. Saha, D. Gupta, M.M. Abu-Omar, A. Modak, A. Bhaumik, J. Catal. 299 (2013) 316–320.
[7] Y. Roman-Leshkov, J.N. Chheda, J.A. Dumesic, Science 312 (2006) 1933–1937.
[8] A. Brandolese, D. Ragno, G. Di Carmine, T. Bernardi, O. Bortolini, P.P. Giovannini, O.G. Pandoli, A. Altomare, A. Massi, Org. Biomol. Chem. 16 (2018) 8955–8964.
[9] J. Lewkowski, Arkivoc (2001) 17–54.
[10] Y.T. Geng, Z. Wang, X.R. Hu, Y. Li, Q.N. Zhang, Y.J. Li, R.G. Wang, L.Q. Zhang, Eur. Polym. J. 114 (2019) 476–484.

[11] J.H. Zhang, J.K. Li, Y.J. Tang, L. Lin, M.N. Long, Carbohydr. Polym. 130 (2015) 420–428.
[12] Z.H. Zhang, K.J. Deng, ACS Catal. 5 (2015) 6529–6544.
[13] T. Werpy, G. Petersen, U.S. Department of Energy, 2004.
[14] R. Fittig, H. Heinzelmann, Chem. Ber. 9 (1876) 1198.
[15] R. Kuhn, K. Dury, Justus Liebigs Ann. Chem. 571 (1951) 44–68.
[16] J. Liu, 2019, http://english.cas.cn/newsroom/research_news/201901/t20190125_204985.shtml
[17] S.E. Davis, L.R. Houk, E.C. Tamargo, A.K. Datye, R.J. Davis, Catal. Today 160 (2011) 55–60.
[18] Y.Y. Gorbanev, S.K. Klitgaard, J.M. Woodley, C.H. Christensen, A. Riisager, ChemSusChem 2 (2009) 672–675.
[19] H.A. Xia, S.Q. Xu, H. Hu, J.H. An, C.Z. Li, RSC Adv. 8 (2018) 30875–30886.
[20] J. Artz, R. Palkovits, ChemSusChem 8 (2015) 3832–3838.
[21] O. Casanova, S. Iborra, A. Corma, ChemSusChem 2 (2009) 1138–1144.
[22] J.Y. Cai, H. Ma, J.J. Zhang, Q. Song, Z.T. Du, Y.Z. Huang, J. Xu, Chem.-Eur. J. 19 (2013) 14215–14223.
[23] K.R. Vuyyuru, P. Strasser, Catal. Today 195 (2012) 144–154.
[24] H.A. Rass, N. Essayem, M. Besson, Green Chem. 15 (2013) 2240–2251.
[25] B. Siyo, M. Schneider, M.M. Pohl, P. Langer, N. Steinfeldt, Catal. Lett. 144 (2014) 498–506.
[26] B. Siyo, M. Schneider, J. Radnik, M.M. Pohl, P. Langer, N. Steinfeldt, Appl. Catal. A 478 (2014) 107–116.
[27] D. Lei, K. Yu, M.R. Li, Y.L. Wang, Q. Wang, T. Liu, P.K. Liu, L.L. Lou, G.C. Wang, S. X. Liu, ACS Catal. 7 (2017) 421–432.
[28] Y.Q. Liu, H.Y. Ma, D. Lei, L.L. Lou, S.X. Liu, W.Z. Zhou, G.C. Wang, K. Yu, ACS Catal. 9 (2019) 8306–8315.
[29] X.M. Liao, J.D. Hou, Y. Wang, H. Zhang, Y. Sun, X.P. Li, S.Y. Tang, K. Kato, M. Yarnauchi, Z. Jiang, Green Chem. 21 (2019) 4194–4203.
[30] C.L. Chen, X.T. Li, L.C. Wang, T. Liang, L. Wang, Y.J. Zhang, J. Zhang, ACS Sustain Chem. Eng. 5 (2017) 11300–11306.
[31] J. Yang, H.C. Yu, Y.B. Wang, F.Y. Qi, H.D. Liu, L.L. Lou, K. Yu, W.Z. Zhou, S.X. Liu, Catal Sci. Technol. 9 (2019) 6659–6668.
[32] C. Megias-Sayago, A. Lolli, D. Bonincontro, A. Penkova, S. Albonetti, F. Cavani, J.A. Odriozola, S. Ivanova, ChemCatChem 12 (2020) 1177–1183.
[33] L.F. Zheng, J.Q. Zhao, Z.X. Du, B.N. Zong, H.C. Liu, Sci. China. Chem. 60 (2017) 950–957.
[34] F. Kerdi, H.A. Rass, C. Pinel, M. Besson, G. Peru, B. Leger, S. Rio, E. Monflier, A. Ponchel, Appl. Catal. A 506 (2015) 206–219.
[35] S. Albonetti, T. Pasini, A. Lolli, M. Blosi, M. Piccinini, N. Dimitratos, J.A. Lopez-Sanchez, D.J. Morgan, A.F. Carley, G.J. Hutchings, F. Cavani, Catal. Today 195 (2012) 120–126.
[36] P. Verdeguer, N. Merat, A. Gaset, J. Mol. Catal. 85 (1993) 327–344.
[37] H.A. Rass, N. Essayem, M. Besson, ChemSusChem 8 (2015) 1206–1217.
[38] Z.Z. Miao, T.X. Wu, J.W. Li, T. Yi, Y.B. Zhang, X.G. Yang, RSC Adv. 5 (2015) 19823–19829.
[39] Z.H. Zhang, J.D. Zhen, B. Liu, K.L. Lv, K.J. Deng, Green Chem. 17 (2015) 1308–1317.
[40] N. Mei, B. Liu, J.D. Zheng, K.L. Lv, D.G. Tang, Z.H. Zhang, Catal. Sci. Technol. 5 (2015) 3194–3202.
[41] B. Liu, Y.S. Ren, Z.H. Zhang, Green Chem. 17 (2015) 1610–1617.
[42] C.M. Zhou, W.R. Shi, X.Y. Wan, Y. Meng, Y. Yao, Z. Guo, Y.H. Dai, C. Wang, Y.H. Yang, Catal. Today 330 (2019) 92–100.
[43] Z.Z. Yang, W. Qi, R.X. Su, Z.M. He, Energy Fuels 31 (2017) 533–541.
[44] A.B. Gawade, A.V. Nakhate, G.D. Yadav, Catal. Today 309 (2018) 119–125.
[45] K.F. Wang, C.L. Liu, K.Y. Sui, C. Guo, C.Z. Liu, ChemBioChem 19 (2018) 654–659.
[46] S. Albonetti, A. Lolli, V. Morandi, A. Migliori, C. Lucarelli, F. Cavani, Appl. Catal. B 163 (2015) 520–530.
[47] M. Kim, Y.Q. Su, A. Fukuoka, E.J.M. Hensen, K. Nakajima, Angew. Chem. Int. Ed. 57 (2018) 8235–8239.
[48] O.R. Schade, K.F. Kalz, D. Neukum, W. Kleist, J.D. Grunwaldt, Green Chem. 20 (2018) 3530–3541.
[49] Q.Q. Li, H.Y. Wang, Z.P. Tian, Y.J. Weng, C.G. Wang, J.R. Ma, C.F. Zhu, W.Z. Li, Q. Y. Liu, L.L. Ma, Catal. Sci. Technol. 9 (2019) 1570–1580.
[50] B.L. Sang, J. Li, X.Q. Tian, F.L. Yuan, Y.J. Zhu, Mol. Catal. 470 (2019) 67–74.
[51] C. Megias-Sayago, A. Lolli, S. Ivanova, S. Albonetti, F. Cavani, J.A. Odriozola, Catal. Today 333 (2019) 169–175.
[52] P.V. Rathod, V.H. Jadhav, ACS Sustain. Chem. Eng. 6 (2018) 5766–5771.
[53] A.D.D. Ferreira, M.D. de Mello, M.A.P. da Silva, Ind. Eng. Chem. Res. 58 (2019) 128–137.
[54] H. Liu, X.J. Cao, T. Wang, J.N. Wei, X. Tang, X.H. Zeng, Y. Sun, T.Z. Lei, S.J. Liu, L. Lin, J. Ind. Eng. Chem. 77 (2019) 209–214.
[55] Z.Z. Miao, Y.B. Zhang, X.Q. Pan, T.X. Wu, B. Zhang, J.W. Li, T. Yi, Z.D. Zhang, X.G. Yang, Catal. Sci. Technol. 5 (2015) 1314–1322.
[56] A. Villa, M. Schiavoni, S. Campisi, G.M. Veith, L. Prati, ChemSusChem 6 (2013) 609–612.
[57] X.Y. Wan, C.M. Zhou, J.S. Chen, W.P. Deng, Q.H. Zhang, Y.H. Yang, Y. Wang, ACS Catal. 4 (2014) 2175–2185.
[58] Y.T. Liao, N.V. Chi, N. Ishiguro, A.P. Young, C.K. Tsung, K.C.W. Wu, Appl. Catal. B 270 (2020) 118805.
[59] A. Lolli, S. Albonetti, L. Utili, R. Amadori, F. Ospitali, C. Lucarelli, F. Cavani, Appl. Catal. A 504 (2015) 408–419.
[60] M. Blosi, S. Ortelli, A.L. Costa, M. Dondi, A. Lolli, S. Andreoli, P. Benito, S. Albonetti, Materials 9 (2016) 550.
[61] D. Bonincontro, F. Fraschetti, C. Squarzoni, L. Mazzocchetti, E. Maccaferri, L. Giorgini, A. Zucchelli, C. Gualandi, M.L. Focarete, S. Albonetti, Processes 8 (2020) 45.
[62] Z.Y. Gui, W.R. Cao, S. Saravanamurugan, A. Riisager, L.F. Chen, Z.W. Qi, ChemCatChem 8 (2016) 3636–3643.
[63] D.J. Chadderdon, L. Xin, J. Qi, Y. Qiu, P. Krishna, K.L. More, W.Z. Li, Green Chem. 16 (2014) 3778–3786.
[64] Q. Wang, W. Hou, S. Li, J.Y. Xie, J. Li, Y. Zhou, J. Wang, Green Chem. 19 (2017) 3820–3830.
[65] H.A. Xia, J.H. An, M. Hong, S.Q. Xu, L. Zhang, S.L. Zuo, Catal. Today 319 (2019) 113–120.
[66] S. Cattaneo, D. Bonincontro, T. Bere, C.J. Kiely, G.J. Hutchings, N. Dimitratos, S. Albonetti, ChemNanoMat 6 (2020) 420–426.
[67] W. Partenheimer, Catal. Today 23 (1995) 69–158.
[68] H. Ban, S.B. Chen, Y.D. Zhang, Y.W. Cheng, L.J. Wang, X. Li, Ind. Eng. Chem. Res. 58 (2019) 19009–19021.
[69] S. Kawasaki, K. Kamata, M. Hara, ChemCatChem 8 (2016) 3247–3253.
[70] E. Hayashi, T. Komanoya, K. Kamata, M. Hara, ChemSusChem 10 (2017) 654–658.
[71] E. Hayashi, Y. Yamaguchi, K. Kamata, N. Tsunoda, Y. Kumagai, F. Oba, M. Hara, J. Am. Chem. Soc. 141 (2019) 890–900.
[72] L.W. Bao, F.Z. Sun, G.Y. Zhang, T.L. Hu, ChemSusChem 13 (2020) 548–555.
[73] X.W. Han, C.Q. Li, X.H. Liu, Q.N. Xia, Y.Q. Wang, Green Chem. 19 (2017) 996–1004.
[74] K.T.V. Rao, J.L. Rogers, S. Souzanchi, L. Dessbesell, M.B. Ray, C.B. Xu, ChemSusChem 11 (2018) 3323–3334.
[75] S. Zhang, X.Z. Sun, Z.H. Zheng, L. Zhang, Catal. Commun. 113 (2018) 19–22.
[76] F. Neatu, R.S. Marin, M. Florea, N. Petrea, O.D. Pavel, V.I. Parvulescu, Appl. Catal. B 180 (2016) 751–757.
[77] K. Yu, Y.Q. Liu, D. Lei, Y.Z. Jiang, Y.B. Wang, Y.J. Feng, L.L. Lou, S.X. Liu, W.Z. Zhou, Catal. Sci. Technol. 8 (2018) 2299–2303.
[78] H. Zhou, H.H. Xu, Y. Liu, Appl. Catal. B 244 (2019) 965–973.
[79] A. Jain, S.C. Jonnalagadda, K.V. Ramanujachary, A. Mugweru, Catal. Commun. 58 (2015) 179–182.
[80] X.H. Zhou, K.H. Song, Z.H. Li, W.M. Kang, H.R. Ren, K.M. Su, M.L. Zhang, B.W. Cheng, Ceram. Int. 45 (2019) 2330–2337.
[81] S. Xu, P. Zhou, Z.H. Zhang, C.J. Yang, B.G. Zhang, K.J. Deng, S. Bottle, H.Y. Zhu, J. Am. Chem. Soc. 139 (2017) 14775–14782.
[82] S. Li, K.M. Su, Z.H. Li, B.W. Cheng, Green Chem. 18 (2016) 2122–2128.
[83] C.V. Nguyen, Y.T. Liao, T.C. Kang, J.E. Chen, T. Yoshikawa, Y. Nakasaka, T. Masuda, K.C.W. Wu, Green Chem. 18 (2016) 5957–5961.
[84] C.L. Chen, J. Zhang, B.S. Zhang, C.L. Yu, F. Peng, D.S. Su, Chem. Commun. 49 (2013) 8151–8153.
[85] S. Verma, M.N. Nadagouda, R.S. Varma, Sci. Rep. 7 (2017) 13596.
[86] M. Jobbagy, A.E. Regazzoni, Appl. Clay Sci. 51 (2011) 366–369.
[87] B.N. Zope, S.E. Davis, R.J. Davis, Top. Catal. 55 (2012) 24–32.
[88] https://www.chemicalbook.com/ChemicalProductProperty_EN_CB6264091.htm
[89] J.H. Xie, J.F. Nie, H.C. Liu, Chin. J. Catal. 35 (2014) 937–944.
[90] G.S. Yi, S.P. Teong, Y.G. Zhang, Green Chem. 18 (2016) 979–983.
[91] N.K. Gupta, S. Nishimura, A. Takagaki, K. Ebitani, Green Chem. 13 (2011) 824–827.
[92] L. Ardemani, G. Cibin, A.J. Dent, M.A. Isaacs, G. Kyriakou, A.F. Lee, C.M.A. Parlett, S.A. Parry, K. Wilson, Chem. Sci. 6 (2015) 4940–4945.
[93] Y.Y. Gorbanev, S. Kegnaes, A. Riisager, Catal. Lett. 141 (2011) 1752–1760.
[94] Y.Y. Gorbanev, S. Kegaens, A. Riisager, Top. Catal. 54 (2011) 1318–1324.
[95] Y.B. Wang, K. Yu, D. Lei, W. Si, Y.J. Feng, L.L. Lou, S.X. Liu, ACS Sustain. Chem. Eng. 4 (2016) 4752–4761.
[96] H. Choudhary, K. Ebitani, Chem. Lett. 45 (2016) 613–615.
[97] C.M. Zhou, W.P. Deng, X.Y. Wan, Q.H. Zhang, Y.H. Yang, Y. Wang, ChemCatChem 7 (2015) 2853–2863.
[98] Z. Gao, R.F. Xie, G.L. Fan, L. Yang, F. Li, ACS Sustain. Chem. Eng. 5 (2017) 5852–5861.
[99] T.Q. Gao, T.Y. Gao, W.H. Fang, Q.E. Cao, Mol. Catal. 439 (2017) 171–179.
[100] W.X. Sun, T.Q. Gao, G.H. Zhu, Q.U. Cao, W.H. Fang, Chemistryselect 5 (2020) 1416–1423.
[101] C.A. Antonyraj, N.T.T. Huynh, K.W. Lee, Y.J. Kim, S. Shin, J.S. Shin, J.K. Cho, J. Chem. Sci. 130 (2018) 156.
[102] X.W. Han, L. Geng, Y. Guo, R. Jia, X.H. Liu, Y.G. Zhang, Y.Q. Wang, Green Chem. 18 (2016) 1597–1604.
[103] X.W. Han, C.Q. Li, Y. Guo, X.H. Liu, Y.G. Zhang, Y.Q. Wang, Appl. Catal. A 526 (2016) 1–8.
[104] C.X. Ke, M.Y. Li, G.L. Fan, L. Yang, F. Li, Chem. -Asian J. 13 (2018) 2714–2722.
[105] D. Bonincontro, A. Lolli, A. Villa, L. Prati, N. Dimitratos, G.M. Veith, L.E. Chinchilla, G.A. Botton, F. Cavani, S. Albonetti, Green Chem. 21 (2019) 4090–4099.
[106] C.L. Chen, J. Zhang, F. Peng, D.S. Su, Mater. Res. Bull. 48 (2013) 3218–3222.
[107] D.S. Su, S. Perathoner, G. Centi, Chem. Rev. 113 (2013) 5782–5816.
[108] P. Sharma, M. Solanki, R.K. Sharma, New J. Chem. 43 (2019) 10601–10609.
[109] B. Frank, R. Blume, A. Rinaldi, A. Trunschke, R. Schlogl, Angew. Chem. Int. Ed. 50 (2011) 10226–10230.
[110] D.V. Chernysheva, V.A. Klushin, A.F. Zubenko, L.S. Pudova, O.A. Kravchenko, V. M. Chernyshev, N.V. Smirnova, Mendeleev. Comm. 28 (2018) 431–433.
[111] E.D. da Silva, W.A. Gonzalez, M.A. Fraga, Green Process. Synth. 5 (2016) 353–364.

[112] D. Bonincontro, A. Lolli, A. Storione, A. Gasparotto, B. Berti, S. Zacchini, N. Dimitratos, S. Albonetti, Appl. Catal. A 588 (2019) 117279.
[113] H. Chen, J.S. Shen, K.Q. Chen, Y. Qin, X.Y. Lu, P.K. Ouyang, J. Fu, Appl. Catal. A 555 (2018) 98–107.
[114] J.S. Shen, H. Chen, K.Q. Chen, Y. Qin, X.Y. Lu, P.K. Ouyang, J. Fu, Ind. Eng. Chem. Res. 57 (2018) 2811–2818.
[115] C.M. Pichler, M.G. Al-Shaal, D. Gu, H. Joshi, W. Ciptonugroho, F. Schuth, ChemSusChem 11 (2018) 2083–2090.
[116] D.K. Mishra, H.J. Lee, J. Kim, H.S. Lee, J.K. Cho, Y.W. Suh, Y. Yi, Y.J. Kim, Green Chem. 19 (2017) 1619–1623.
[117] W. Partenheimer, V.V. Grushin, Adv. Synth. Catal. 343 (2001) 102–111.
[118] T.Y. Gao, J. Chen, W.H. Fang, Q.E. Cao, W.P. Su, F. Dumeignil, J. Catal. 368 (2018) 53–68.
[119] M. Ventura, F. Nocito, E. de Giglio, S. Cometa, A. Altomare, A. Dibenedetto, Green Chem. 20 (2018) 3921–3926.
[120] M. Ventura, M. Aresta, A. Dibenedetto, ChemSusChem 9 (2016) 1096–1100.
[121] X.L. Tong, L.N. Yu, H. Chen, X.L. Zhuang, S.Y. Liao, H.G. Cui, Catal. Commun. 90 (2017) 91–94.
[122] M. Ventura, F. Lobefaro, E. de Giglio, M. Distaso, F. Nocito, A. Dibenedetto, ChemSusChem 11 (2018) 1305–1315.
[123] T.Y. Gao, Y.X. Yin, W.H. Fang, Q. Cao, Mol. Catal. 450 (2018) 55–64.
[124] M.A. Lilga, R.T. Hallen, M. Gray, Top. Catal. 53 (2010) 1264–1269.
[125] F. Liguori, P. Barbaro, N. Calisi, ChemSusChem 12 (2019) 2558–2563.
[126] L. Du, Y.Y. Shao, J.M. Sun, G.P. Yin, C.Y. Du, Y. Wang, Catal. Sci. Technol. 8 (2018) 3216–3232.
[127] W.J. Liu, L.N. Dang, Z.R. Xu, H.Q. Yu, S. Jin, G.W. Huber, ACS Catal. 8 (2018) 5533–5541.
[128] R. Francke, R.D. Little, Chem. Soc. Rev. 43 (2014) 2492–2521.
[129] H.S. Awad, N.A. Galwa, Chemosphere 61 (2005) 1327–1335.
[130] Y. Jiao, Y. Zheng, M.T. Jaroniec, S.Z. Qiao, Chem. Soc. Rev. 44 (2015) 2060–2086.
[131] O. Kawana, Y. Nakamura, Y. Yoshihiro, Nippon Kagaku Kaishi (1983) 1747–1752.
[132] G. Grabowski, J. Lewkowski, R. Skowronski, Electrochim. Acta 36 (1991), 1995 1995.
[133] B. You, N. Jiang, X. Liu, Y.J. Sun, Angew. Chem. Int. Ed. 55 (2016) 9913–9917.
[134] N. Jiang, B. You, R. Boonstra, I.M.T. Rodriguez, Y.J. Sun, ACS Energy Lett. 1 (2016) 386–390.
[135] B. You, X. Liu, N. Jiang, Y.J. Sun, J. Am. Chem. Soc. 138 (2016) 13639–13646.
[136] B. You, X. Liu, X. Liu, Y.J. Sun, ACS Catal. 7 (2017) 4564–4570.
[137] S. Barwe, J. Weidner, S. Cychy, D.M. Morales, S. Dieckhofer, D. Hiltrop, J. Masa, M. Muhler, W. Schuhmann, Angew. Chem. Int. Ed. 57 (2018) 11460–11464.
[138] J. Weidner, S. Barwe, K. Sliozberg, S. Piontek, J. Masa, U.P. Apfel, W. Schuhmann, Beilstein J. Org. Chem. 14 (2018) 1436–1445.
[139] P.L. Zhang, X. Sheng, X.Y. Chen, Z.Y. Fang, J. Jiang, M. Wang, F.S. Li, L.Z. Fan, Y.S. Ren, B.B. Zhang, B.J.J. Timmer, M.S.G. Ahlquist, L.C. Sun, Angew. Chem. Int. Ed. 58 (2019) 9155–9159.
[140] L.F. Gao, Y. Bao, S.Y. Gan, Z.H. Sun, Z.Q. Song, D.X. Han, F.H. Li, L. Niu, ChemSusChem 11 (2018) 2547–2553.
[141] M.J. Kang, H. Park, J. Jegal, S.Y. Hwang, Y.S. Kang, H.G. Cha, Appl. Catal. B 242 (2019) 85–91.
[142] S.Q. Li, X. Sun, Z.H. Yao, X. Zhong, Y.Y. Coo, Y.L. Liang, Z.Z. Wei, S.W. Deng, G.L. Zhuang, X.N. Li, J.G. Wang, Adv. Funct. Mater. 29 (2019) 1904780.
[143] N.N. Zhang, Y.Q. Zou, L. Tao, W. Chen, L. Zhou, Z.J. Liu, B. Zhou, G. Huang, H.Z. Lin, S.Y. Wang, Angew. Chem. Int. Ed. 58 (2019) 15895–15903.
[144] B.J. Taitt, D.H. Nam, K.S. Choi, ACS Catal. 9 (2019) 660–670.
[145] R. Latsuzbaia, R. Bisselink, A. Anastasopol, H. van der Meer, R. van Heck, M.S. Yague, M. Zijlstra, M. Roelands, M. Crockatt, E. Goetheer, E. Giling, J. Appl. Electrochem. 48 (2018) 611–626.
[146] D.H. Nam, B.J. Taitt, K.S. Choi, ACS Catal. 8 (2018) 1197–1206.
[147] H. Chen, J.T. Wang, Y. Yao, Z.H. Zhang, Z.Z. Yang, J. Li, K.Q. Chen, X.Y. Lu, P.K. Ouyang, J. Fu, ChemElectroChem 6 (2019) 5797–5801.
[148] L.F. Gao, Z.B. Liu, J.L. Ma, L.J. Zhong, Z.Q. Song, J.A. Xu, S.Y. Gan, D.X. Han, L. Niu, Appl. Catal. B 261 (2020) 118235.
[149] X.H. Deng, X.M. Kang, M. Li, K. Xiang, C. Wang, Z.P. Guo, J.J. Zhang, X.Z. Fu, J.L. Luo, J. Mater. Chem. A 8 (2020) 1138–1146.
[150] S.R. Kubota, K.S. Choi, ChemSusChem 11 (2018) 2138–2145.
[151] Y. Kwon, Y.Y. Birdja, S. Raoufmoghaddam, M.T.M. Koper, ChemSusChem 8 (2015) 1745–1751.
[152] Y. Kwon, E. de Jong, S. Raoufmoghaddam, M.T.M. Koper, ChemSusChem 6 (2013) 1659–1667.
[153] Z.Q. Zhou, C.L. Chen, M.R. Gao, B.W. Xia, J. Zhang, Green Chem. 21 (2019) 6699–6706.
[154] G.C. Yang, Y.Q. Jiao, H.J. Yan, Y. Xie, A.P. Wu, X. Dong, D.Z. Guo, C.G. Tian, H.G. Fu, Adv. Mater. 32 (2020) 2000455.
[155] J.S. Wang, Q.H. Wei, Q.X. Ma, Z.Y. Guo, F.F. Qin, Z.R. Ismagilov, W.Z. Shen, Appl. Catal. B 263 (2020) 118339.
[156] Y.R. Zhang, B.X. Wang, L. Qin, Q. Li, Y.M. Fan, Green Chem. 21 (2019) 1108–1113.
[157] W.Z. Li, X. Chadderdon, D. Chadderdon, Abstr. Pap. Am. Chem. S. 257 (2019) 30.
[158] X.H. Chadderdon, D.J. Chadderdon, T. Pfennig, B.H. Shanks, W. Li, Green Chem. 22 (2019) 6210–6219.
[159] X. Zhang, M.M. Han, G.Q. Liu, G.Z. Wang, Y.X. Zhang, H.M. Zhang, H.J. Zhao, Appl. Catal. B 244 (2019) 899–908.
[160] Q. Qin, T. Heil, J. Schmidt, M. Schmallegger, G. Gescheidt, M. Antonietti, M. Oschatz, ACS Appl. Energy Mater. 2 (2019) 8359–8365.
[161] H.G. Cha, K.S. Choi, Nat. Chem. 7 (2015) 328–333.
[162] A.C. Cardiel, B.J. Taitt, K.S. Choi, ACS Sustain. Chem. Eng. 7 (2019) 11138–11149.
[163] D.J. Chadderdon, L.P. Wu, Z.A. McGraw, M. Panthani, W.Z. Li, ChemElectroChem 6 (2019) 3387–3392.
[164] G.Q. Han, Y.H. Jin, R.A. Burgess, N.E. Dickenson, X.M. Cao, Y.J. Sun, J. Am. Chem. Soc. 139 (2017) 15584–15587.
[165] D.A. Gonzalez-Casamachin, J. Rivera De la Rosa, C.J. Lucio-Ortiz, L. Sandoval-Rangel, C.D. García, Chem. Eng. J. 393 (2020) 124699.
[166] S.E. Davis, B.N. Zope, R.J. Davis, Green Chem. 14 (2012) 143–147.
[167] S. Siankevich, G. Savoglidis, Z.F. Fei, G. Laurenczy, D.T.L. Alexander, N. Yan, P.J. Dyson, J. Catal. 315 (2014) 67–74.
[168] X.Q. Liu, X.G. Duan, W. Wei, S.B. Wang, B.J. Ni, Green Chem. 21 (2019) 4266–4289.
[169] M. Kroger, U. Prusse, K.D. Vorlop, Top. Catal. 13 (2000) 237–242.
[170] M.L. Ribeiro, U. Schuchardt, Catal. Commun. 4 (2003) 83–86.
[171] S.G. Wang, Z.H. Zhang, B. Liu, ACS Sustain. Chem. Eng. 3 (2015) 406–412.